






ARTICLE

VE-cadherin endocytosis controls vascular integrity and patterning during development

Cynthia M. Grimsley-Myers¹, Robin H. Isaacson¹, Chantel M. Cadwell¹, Jazmin Campos¹, Marina S. Hernandez², Kenneth R. Myers¹, Tadahiko Seo¹, William Giang¹, Kathy K. Griendling², and Andrew P. Kowalczyk³

Tissue morphogenesis requires dynamic intercellular contacts that are subsequently stabilized as tissues mature. The mechanisms governing these competing adhesive properties are not fully understood. Using gain- and loss-of-function approaches, we tested the role of p120-catenin (p120) and VE-cadherin (VE-cad) endocytosis in vascular development using mouse mutants that exhibit increased (VE-cad^{GGG/GGG}) or decreased (VE-cad^{DEE/DEE}) internalization. VE-cad^{GGG/GGG} mutant mice exhibited reduced VE-cad-p120 binding, reduced VE-cad levels, microvascular hemorrhaging, and decreased survival. By contrast, VE-cad^{DEE/DEE} mutants exhibited normal vascular permeability but displayed microvascular patterning defects. Interestingly, VE-cad^{DEE/DEE} mutant mice did not require endothelial p120, demonstrating that p120 is dispensable in the context of a stabilized cadherin. In vitro, VE-cad^{DEE} mutant cells displayed defects in polarization and cell migration that were rescued by uncoupling VE-cad^{DEE} from actin. These results indicate that cadherin endocytosis coordinates cell polarity and migration cues through actin remodeling. Collectively, our results indicate that regulated cadherin endocytosis is essential for both dynamic cell movements and establishment of stable tissue architecture.

Introduction

Collective cell movements are a central feature of tissue patterning throughout embryonic development and are essential for wound healing in adult organisms (Friedl and Gilmour, 2009; Mayor and Etienne-Manneville, 2016). Significant advances have been made toward understanding the signaling and growth factor pathways that contribute to these processes. However, we lack a comprehensive understanding of how cells engage in adhesive intercellular contacts that are adequately dynamic to allow for collective cell movement and yet sufficiently stable to maintain tissue architecture. In the present study, we used gain- and loss-of-function mouse genetic approaches to understand how endocytosis governs cadherin dynamics to permit both angiogenic vascular remodeling and vascular cohesion during development.

Blood vessel formation is fundamental to embryonic development and organogenesis as well as numerous pathological conditions ranging from diabetes to cancer (Carmeliet and Jain, 2011; Fallah et al., 2019; Folkman, 2007). Formation of the hierarchically branched vascular network is driven largely by angiogenic sprouting of endothelial cells from preexisting vessels during early development (Chappell et al., 2011; Potente et al., 2011). Sprout formation is a complex morphogenetic

process that entails the polarization and collective migration of endothelial cells coordinated with proliferation, differentiation, and lumen formation (Betz et al., 2016; Geudens and Gerhardt, 2011; Schuermann et al., 2014). During sprouting, contacts between neighboring cells must remain tight to maintain cohesion. However, sprouting is also highly dynamic and involves cell intercalations and coordinated cell shape changes requiring constant remodeling of cell–cell contacts (Arima et al., 2011; Bentley et al., 2014; Jakobsson et al., 2010; Szyborska and Gerhardt, 2018).

Vascular endothelial cadherin (VE-cad) is the principal cell–cell adhesion molecule of the endothelial adherens junction (Giannotta et al., 2013; Lagendijk and Hogan, 2015). The extracellular domain of VE-cad mediates adhesion through homophilic trans interactions, whereas its cytoplasmic tail associates with the actin cytoskeleton, providing mechanical strength to the adhesive junction (Dejana and Vestweber, 2013; Oas et al., 2013; Shapiro and Weis, 2009). VE-cad is expressed selectively in vascular and lymphatic endothelial cells and has been implicated in multiple aspects of blood vessel formation (Abraham et al., 2009; Gaengel et al., 2012; Helker et al., 2013; Lenard et al., 2013; Sauter et al., 2014). Mice lacking VE-cad die

¹Department of Cell Biology, Emory University School of Medicine, Atlanta, GA; ²Division of Cardiology, Department of Medicine, Emory University School of Medicine, Atlanta, GA; ³Department of Cell Biology, Department of Dermatology, and Winship Cancer Institute, Emory University School of Medicine, Atlanta, GA.

Correspondence to Andrew P. Kowalczyk: akowalc@emory.edu; Cynthia M. Grimsley-Myers: cynthiamyers@emory.edu.

© 2020 Grimsley-Myers et al. This article is distributed under the terms of an Attribution–Noncommercial–Share Alike–No Mirror Sites license for the first six months after the publication date (see <http://www.rupress.org/terms/>). After six months it is available under a Creative Commons License (Attribution–Noncommercial–Share Alike 4.0 International license, as described at <https://creativecommons.org/licenses/by-nc-sa/4.0/>).

during midembryogenesis owing to the disintegration of nascent vessels (Carmeliet et al., 1999; Crosby et al., 2005; Gory-Fauré et al., 1999), underscoring the importance of cadherin-mediated adhesion to vascular development. Importantly, VE-cad adhesion is likely to be dynamically regulated during angiogenesis. Computational modeling and analysis of embryoid bodies and developing mouse vessels suggested that VE-cad is dynamically regulated as endothelial cells migrate collectively during angiogenesis (Arima et al., 2011; Bentley et al., 2014; Neto et al., 2018). These studies suggest that VE-cad endocytosis might contribute to collective migration and blood vessel morphogenesis in vivo.

The armadillo protein p120-catenin (p120) is a central regulator of classic cadherin trafficking. p120 binds to the juxta-membrane domain (JMD) in the cadherin tail and potently inhibits cadherin endocytosis and degradation by physically masking various endocytic signals (Cadwell et al., 2016; Ishiyama et al., 2010; Nanes et al., 2012). Tissue-specific knockout of p120 in mice leads to decreased cadherin levels and morphogenetic defects in a variety of tissues (Davis and Reynolds, 2006; Elia et al., 2006; Hendley et al., 2015; Kurley et al., 2012; Marciano et al., 2011; Perez-Moreno et al., 2006), including the developing vasculature (Oas et al., 2010). However, p120 also performs cadherin-independent functions in the regulation of Rho family GTPases and gene transcription (Duñach et al., 2017; Kourtidis et al., 2013). Thus, p120 appears to play cadherin-dependent and -independent functions. However, the relative importance of these different activities of p120 to tissue morphogenesis is poorly understood.

We previously reported that p120 binding physically masks and inhibits a highly conserved 3-aa endocytic signal (DEE) within the p120-binding domain of VE-cad. Dissociation of p120 from the cadherin tail exposes the DEE motif and allows for cadherin internalization, whereas mutation of the DEE motif to alanine residues prevents VE-cad endocytosis (Garrett et al., 2017; Nanes et al., 2012). Structural studies of E-cadherin suggest a similar mechanism by which p120 binding could inhibit a dileucine endocytic motif (Ishiyama et al., 2010). Although the role of p120 in regulating cadherin internalization is well established in mammalian cell culture model systems, data from *Drosophila* models suggest that p120 binding to cadherin is dispensable for fly development (Myster et al., 2003; Pacquelet et al., 2003). In addition, a recent report suggested a role for p120 in mediating cadherin endocytosis rather than inhibiting cadherin internalization (Bulgakova and Brown, 2016). Other studies in flies suggest that dissociation of p120 from *Drosophila* E-cadherin leads to increased E-cadherin turnover (Iyer et al., 2019). Thus, different experimental model systems have yielded conflicting views on the requirements for p120 binding to cadherin, and no vertebrate models of a cadherin mutant deficient in either p120 binding or endocytosis have been reported.

In the present study, we used a series of gain- and loss-of-function mouse genetic approaches to directly test the role of the cadherin-p120 catenin complex and cadherin endocytosis in vertebrate development. We generated homozygous VE-cad mutants lacking the DEE endocytic signal (VE-cad^{DEE/DEE}) and/or adjacent residues needed for p120 binding (VE-cad^{GGG/GGG}).

We found that p120 binding to the VE-cad tail is essential for vessel integrity and for vascular barrier function. However, p120 binding to VE-cad can be rendered dispensable by mutating the DEE endocytic motif to eliminate cadherin endocytosis. Similarly, the VE-cad^{DEE/DEE} mutant can rescue the embryonic lethality associated with the p120-null phenotype, demonstrating that the essential function of p120 is to bind and stabilize cadherin at the cell surface. However, we also found that cadherin endocytosis is needed for normal vessel patterning. Homozygous VE-cad^{DEE/DEE} mutants exhibited impaired angiogenesis in multiple microvascular tissue beds and impaired migration in ex vivo and in vitro migration assays. Further, we show that VE-cad endocytosis is required for actin-dependent polarization of endothelial cells before collective cell movement. These findings demonstrate that p120 regulation of cadherin endocytosis is an essential mechanism that governs the plasticity of cell-cell contacts during vertebrate development, and that cadherin endocytosis is integrated with polarity cues to regulate cell migration and angiogenesis.

Results

Generation of VE-cad mutant alleles with disrupted p120 binding and altered endocytic rates

To determine the roles of p120 binding and VE-cad endocytosis in blood vessel development and endothelial function in vivo, we used the CRISPR/Cas9 system to create a series of mouse knock-in VE-cad mutants with disrupted p120 binding and altered endocytic rates, as summarized in Fig. 1. These mutants allowed us to dissect the specific roles of both p120 binding and VE-cad endocytosis in a mammalian in vivo system using endogenous VE-cad expression levels. First, we mutated highly conserved contiguous GGG residues within the core p120-binding domain to alanine residues (designated VE-cad^{GGG}; Fig. 1, A and B). Mutation of these GGG residues prevents p120 binding, leading to exposure of the DEE endocytic motif and cadherin destabilization (Nanes et al., 2012). Second, we mutated the DEE residues comprising the endocytic motif (designated VE-cad^{DEE}; Fig. 1, A and B). Replacement of these residues with alanine residues leads to a dramatic decrease in constitutive endocytosis of VE-cad from the plasma membrane (Nanes et al., 2012). The DEE mutations also lead to reduced p120-binding, since this motif lies within the p120-binding domain (Nanes et al., 2012). Finally, in the process of making the above mutants, we generated the VE-cad^{ΔJMD} allele. This allele contains an in-frame, 11-aa deletion in the core p120 binding domain comprising both the DEE endocytic motif and the GGG residues (Fig. 1, A and B). This deletion should therefore completely abrogate both DEE-mediated endocytosis and p120 binding. Founder mice for all strains were identified by PCR/restriction fragment length polymorphism analysis and confirmed by Sanger sequencing (Fig. 1 C).

p120 binding to VE-cad is required for vessel integrity and survival

We first sought to determine whether p120 binding to VE-cad is required for vascular morphogenesis and endothelial function in vivo. Heterozygous VE-cad^{GGG/+} mice were viable and fertile and appeared grossly normal. Although genotyping at postnatal

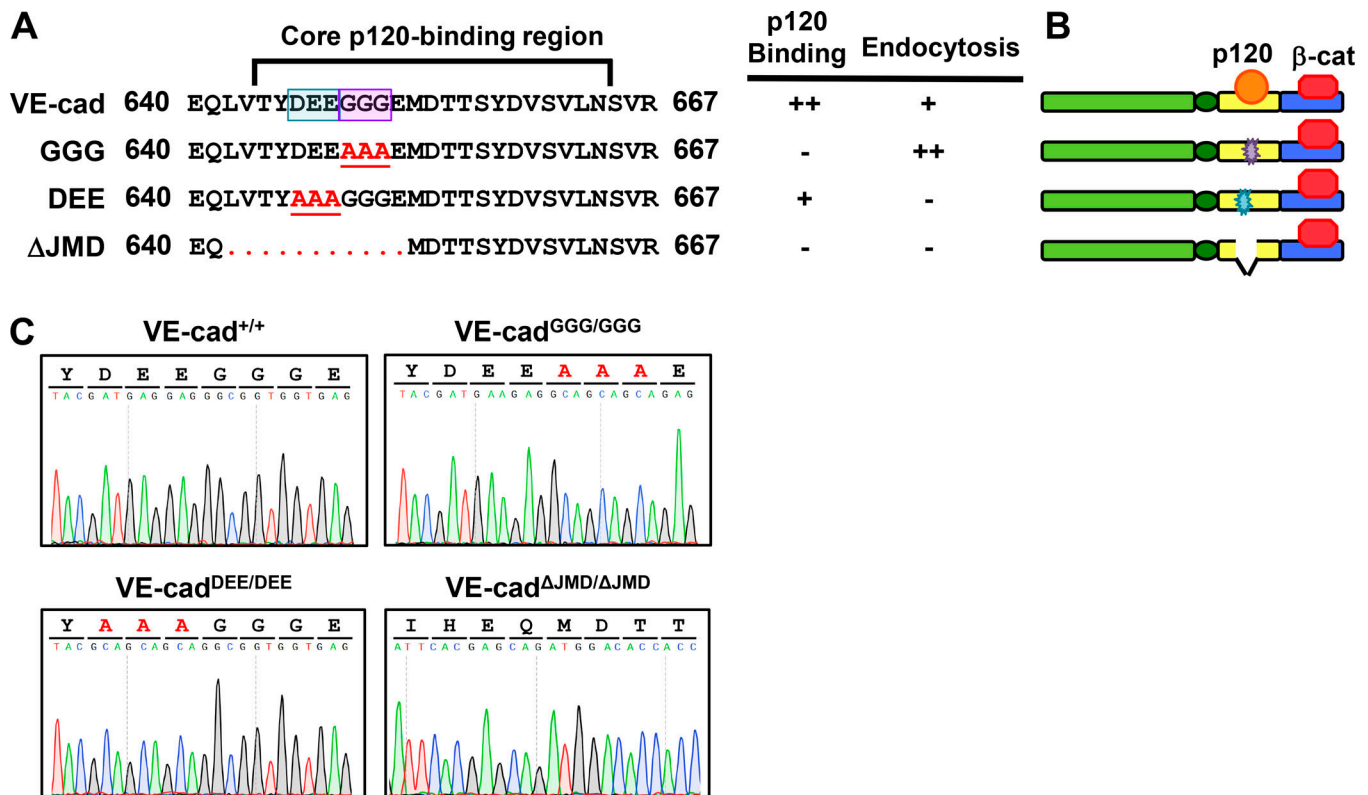


Figure 1. **CRISPR-generated VE-cad mouse mutants.** (A) Amino acid sequence of WT VE-cad core p120-binding domain and mutants analyzed in this study. The WT allele binds p120 and undergoes endocytosis upon p120 dissociation. The VE-cad^{GGG} allele contains alanine substitutions of GGG residues (purple box), which disrupt p120 binding, leading to increased endocytosis. The VE-cad^{DEE} endocytic mutant, with mutated DEE residues (blue box), exhibits partially reduced p120 binding, yet fails to undergo endocytosis. The ΔJMD endocytic mutant contains an 11-aa deletion comprising the DEE signal and surrounding residues, and also fails to bind p120 or undergo endocytosis. (B) Schematic representations of the VE-cad mutants in A. (C) Sanger sequencing chromatograms of the indicated VE-cadherin homozygous mutant mice.

day 0 (P0) revealed that homozygous VE-cad^{GGG/GGG} mutant mice were born at Mendelian ratios (25.4% of 126 pups), these homozygous mutants often died shortly after birth. Dead VE-cad^{GGG/GGG} mutant neonates were frequently observed with visible subcutaneous spots of pooled blood, consistent with leaky blood vessels. Genotyping of offspring ~1 wk after birth revealed that ~30% of VE-cad^{GGG/GGG} mutants die during this period, indicating early postnatal lethality with partial penetrance (Fig. 2 A). We additionally noted that surviving VE-cad^{GGG/GGG} mutants exhibited smaller body size than WT littermates (Fig. 2, B and C). To further examine the lethality phenotype, we crossed VE-cad^{GGG/GGG} mice with heterozygous mice containing a null VE-cad allele (VE-cad^{STOP/+}). This allele contains an early STOP codon at aa 647 and thus lacks the entire β-catenin-binding domain (CBD), leading to a nonfunctional allele (Carmeliet et al., 1999). Although heterozygous VE-cad^{STOP/+} mice are normal and viable, matings with VE-cad^{GGG/GGG} mutants yielded no viable VE-cad^{GGG/STOP} offspring (Fig. S1 A). This complete embryonic lethality of VE-cad^{GGG/STOP} mice further supports a reduced function of the GGG mutant allele and indicates that the binding of p120 is critical for VE-cad function during development.

Because we observed hemorrhages in newborn VE-cad^{GGG/GGG} mutants, we analyzed the macroscopic appearance

of VE-cad^{GGG/GGG} embryos at embryonic day 12.5 (E12.5) to ascertain if hemorrhaging also occurred embryonically. Although blood vessel organization in mutants appeared grossly normal, hemorrhaging was noted in some VE-cad^{GGG/GGG} embryos (Fig. 2 D). The bleeding was localized primarily in the head of the mutant embryos, although blood spots were also visualized in the limbs and other regions along the body wall. We also analyzed bleeding in the retina of VE-cad^{GGG/GGG} mutants at P3, a time point during early formation of the superficial vascular plexus. Although avascular at birth, the mouse retina becomes vascularized in a highly reproducible manner over the first 10 d after birth. Blood vessels form at the optic nerve at the center and then grow outward radially over the surface of the retina by sprouting angiogenesis (Fruttiger, 2007). In the retinas of VE-cad^{GGG/GGG} mutants, we observed increased multifocal bleeding (Fig. 2 D). These blood spots were primarily localized around the growing vascular front of the plexus, where vessels are newly formed and less stable compared with those toward the center of the plexus. Quantitation revealed a fivefold increase in blood spot area in the retinas of VE-cad^{GGG/GGG} mutants compared with WT littermates (Fig. S1 B). The blood leakage and partial lethality in VE-cad^{GGG/GGG} mutants was suggestive of an underlying endothelial integrity defect. Therefore, we assessed vascular permeability in surviving VE-cad^{GGG/GGG} mutants in

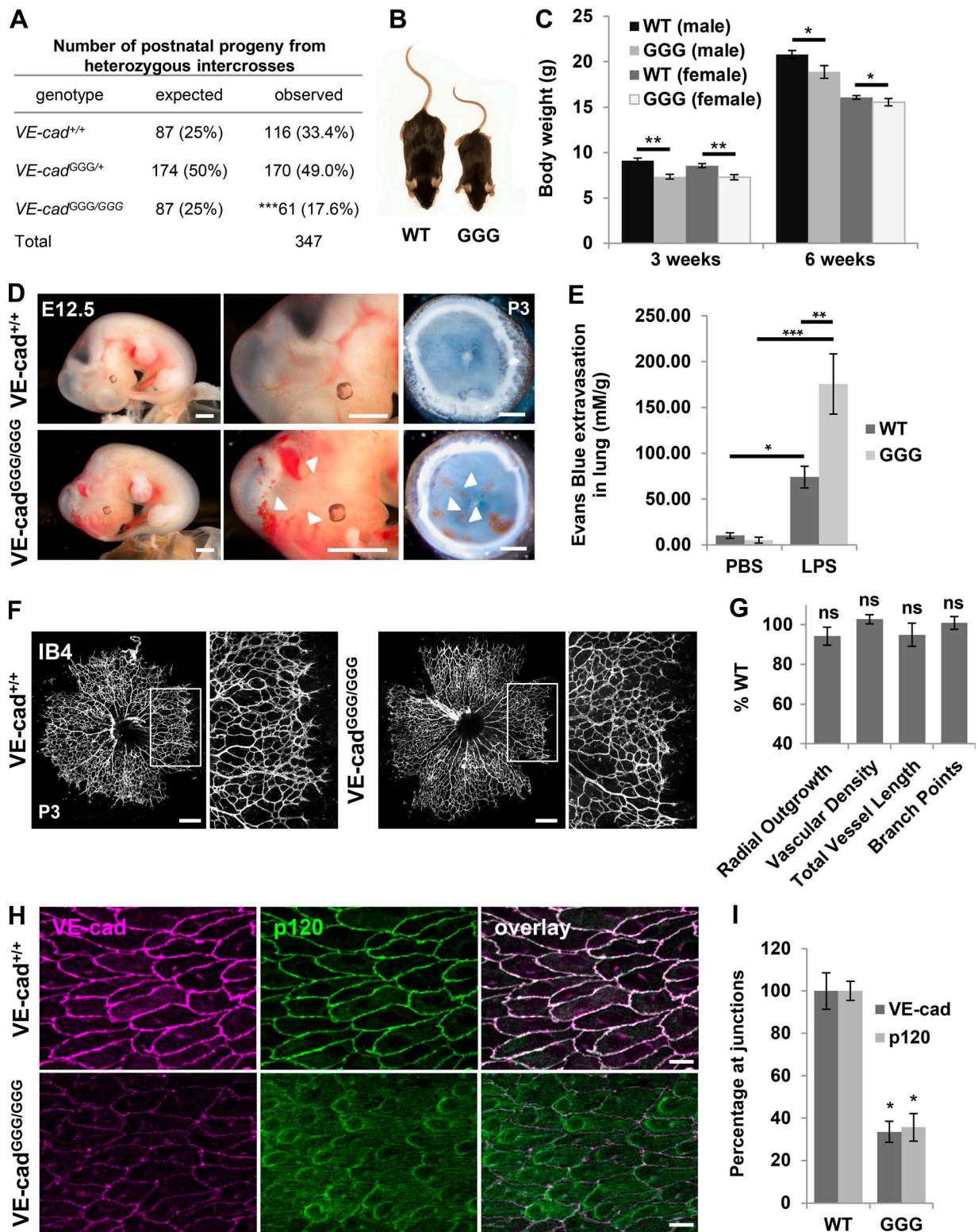


Figure 2. **Decreased VE-cad levels, lethality, and permeability defects in VE-cad GGG mutant mice lacking p120 binding.** (A) Genotyping analysis of postnatal offspring from *VE-cad^{GGG/+}* intercrosses reveals a less than expected number of *VE-cad^{GGG/GGG}* homozygous mutants, indicating partial lethality. Genotyping was performed between P6 and P8, and the expected number of mice was based on the total number of mice and expected Mendelian ratios. ***, $P < 0.001$ in χ^2 analysis. (B) Image of male *VE-cad^{+/+}* and *VE-cad^{GGG/GGG}* littermates at 6 wk of age illustrating small size of *VE-cad^{GGG/GGG}* mutants. (C) Decreased body weight in *VE-cad* GGG mutant mice at 3 and 6 wk. Body weight was assessed in *VE-cad^{+/+}* and *VE-cad^{GGG/GGG}* males and females. Results are shown as mean \pm SEM. *, $P < 0.05$; **, $P < 0.001$, *t* test. (D) Left and middle: Gross examination of *VE-cad^{+/+}* (top) and *VE-cad^{GGG/GGG}* mutant (bottom) whole embryos at E12.5. Variable size hemorrhages (arrows) were observed in the *VE-cad^{GGG/GGG}* embryos, which are shown at larger magnification in the middle panels. Right: Fixed eye cups from *VE-cad^{+/+}* and *VE-cad^{GGG/GGG}* mutant mice at P3. Larger and more frequent hemorrhages (arrows) were observed in

the retinas of VE-cad^{GGG/GGG} mutants compared with littermates. Scale bar, left and middle: 1 mm; right: 0.3 mm. **(E)** Increased vascular permeability in VE-cad^{GGG/GGG} mutant mice. Lung permeability in 3-mo-old mice in response to LPS treatment was assessed by the Evans blue dye method 6 h after treatment. The lungs were harvested, and dye extravasation was quantified spectrophotometrically and normalized to lung dry weight. The bar graph represents means \pm SEM with six to seven mice per group. Two-way ANOVA, *, $P < 0.0437$; ***, $P < 0.0001$; **, $P < 0.0037$. **(F)** Visualization of the retinal vasculature by isolectin-B4 staining at P3 revealed normal blood vessel patterning in VE-cad^{GGG/GGG} mutant retinas (right) compared with VE-cad^{+/+} littermates (left). Panels on the right show higher magnification of the boxed region at the vessel front in left panels. Scale bar: 300 μ m. **(G)** Quantitation of vascular parameters at the vessel front in VE-cad^{GGG/GGG} mutant retinas at P3. Data are presented as percentage of WT littermate control and represent mean \pm SEM; $n = 5$ independent litters. ns, not significant, paired t test. **(H)** Aorta en face preparations from VE-cad^{+/+} and VE-cad^{GGG/GGG} adult mice immunostained for VE-cad (magenta) and p120 (green). VE-cad levels at cell–cell junctions are significantly decreased in the VE-cad^{GGG/GGG} p120-binding mutant, and p120 localization shifts from the cell–cell junctions to the cytoplasm. Scale bar: 20 μ m. **(I)** Quantitation of VE-cad and p120 levels at cell–cell junctions in the aortas of VE-cad^{+/+} and VE-cad^{GGG/GGG} mice. Levels were quantitated from four independent experiments with four to six images per animal and are shown as the relative mean \pm SEM. *, $P < 0.05$, Mann–Whitney U test.

response to lipopolysaccharide (LPS) stimulation using the Evans blue method (Radu and Chernoff, 2013). Under control conditions, we observed no significant differences in permeability between WT and VE-cad^{GGG/GGG} mutants. In response to LPS, however, extravasation of Evans blue dye in the lungs was significantly higher in VE-cad^{GGG/GGG} mutants than in WT mice (74 vs. 176 mM/g; $P < 0.005$; Fig. 2 E). These data, together with the presence of hemorrhaging, indicate an essential role for p120 binding in the establishment and maintenance of endothelial barrier function and resistance to induced vascular leak.

To investigate whether loss of p120 binding in VE-cad^{GGG/GGG} mutants may be associated with decreased vessel sprouting and branching, we assessed vascular development in VE-cad^{GGG/GGG} mutants in the postnatal retina by whole-mount staining with isolectin B4. Surprisingly, we observed no gross vascular patterning changes (Fig. 2 F). Quantitation revealed no significant differences in radial outgrowth, vascular density, vessel length, or branching between VE-cad^{GGG/GGG} mutants and WT littermates (Fig. 2 G). Thus, the formation of vessels appeared normal in VE-cad^{GGG/GGG} mutants despite hemorrhage and leak, indicating that p120 binding to VE-cad is not essential for vascular patterning.

To verify that p120 binding to VE-cad was disrupted by the GGG mutation, we examined VE-cad and p120 localization in endothelial cells in WT and VE-cad^{GGG/GGG} mutants by immunostaining en face preparations of adult aorta. In WT mice, we observed intense VE-cad and p120 border staining at endothelial cell junctions (Fig. 2 H). In contrast, p120 was absent at cell–cell borders in the aorta of VE-cad^{GGG/GGG} mice, and VE-cad levels at cell junctions were dramatically reduced (Fig. 2, H and I). Western blot analysis of dermal endothelial cells isolated from VE-cad^{GGG/GGG} mutants revealed decreased VE-cad levels but no changes in p120 (Fig. S1, C and D). There was also a similar (69%) decrease in the levels of β -catenin at cell borders in the mutants, consistent with the decrease in VE-cad levels (Fig. S1, E and F). Because N-cadherin (N-cad) has been shown to partially compensate for VE-cad in certain contexts (Gentil-dit-Maurin et al., 2010; Giampietro et al., 2012), we also immunostained for N-cad in VE-cad^{GGG/GGG} mutant aortas but failed to observe any up-regulation of N-cad at cell borders (not depicted). Collectively, these data indicate that the loss of p120 binding to the VE-cad cytoplasmic domain leads to severe reductions in VE-cad levels and compromised endothelial barrier function, but no obvious vascular patterning defects.

Deletion of VE-cad DEE endocytic motif restores VE-cad levels and endothelial integrity in the absence of p120 binding

We hypothesized that VE-cad^{GGG/GGG} mutants display decreased levels of VE-cad at junctions owing to the inability of p120 to bind VE-cad and block endocytosis. One way to test this hypothesis would be to simultaneously disrupt both p120 binding and DEE-mediated endocytosis and determine if VE-cad levels are restored. During the process of engineering our mouse strains, we generated a mutant with an in-frame, 11-aa deletion encompassing both the DEE residues and GGG residues (VE-cad ^{Δ JMD/ Δ JMD}; Fig. 1, A–C). We hypothesized that this deletion should prevent both p120 binding and DEE-mediated endocytosis. In the aorta of VE-cad ^{Δ JMD/ Δ JMD} mutants, p120 exhibited a cytoplasmic/perinuclear pattern in endothelial cells, reminiscent of VE-cad^{GGG/GGG} mutants and consistent with the inability of the VE-cad ^{Δ JMD/ Δ JMD} mutant to bind p120 (Fig. 3, A and B). However, in contrast to the VE-cad^{GGG/GGG} mutant, VE-cad levels at endothelial cell–cell junctions in VE-cad ^{Δ JMD/ Δ JMD} mutants were normal (Fig. 3, A and B), despite the lack of p120 binding. Similarly, we observed no change in β -catenin levels at cell borders in VE-cad ^{Δ JMD/ Δ JMD} mutants (Fig. 3, A and B). Total cellular levels of VE-cad and p120 were also normal in Western blots of VE-cad ^{Δ JMD/ Δ JMD} mutant cell lysates (Fig. S1, C and D). Thus, deletion of the DEE endocytic motif prevents the down-regulation of VE-cad at cell junctions associated with lack of p120 binding. These data confirm the dual function of the cadherin JMD in p120 binding and endocytic control. Consistent with this interpretation, VE-cad ^{Δ JMD/ Δ JMD} mutants appeared grossly normal and lacked the partial lethality and hemorrhaging observed in VE-cad^{GGG/GGG} mutants (Fig. 3, C and D; and Fig. S2 A). Together, these data indicate that p120 binding to VE-cad is required for normal vessel development and function, but can be rendered dispensable in the context of a VE-cad mutant that is resistant to endocytosis.

Mutation of DEE endocytic motif partially rescues the p120-knockout phenotype

The normal growth and development of the VE-cad ^{Δ JMD/ Δ JMD} mutants indicate that p120 binding to VE-cad is not required for survival and normal vessel development. Although p120 is not bound to VE-cad in the VE-cad ^{Δ JMD/ Δ JMD} mutants, p120 is still present in the endothelial cells and could carry out other functions independently of cadherin binding. In previous studies, we showed that deletion of endothelial p120 resulted

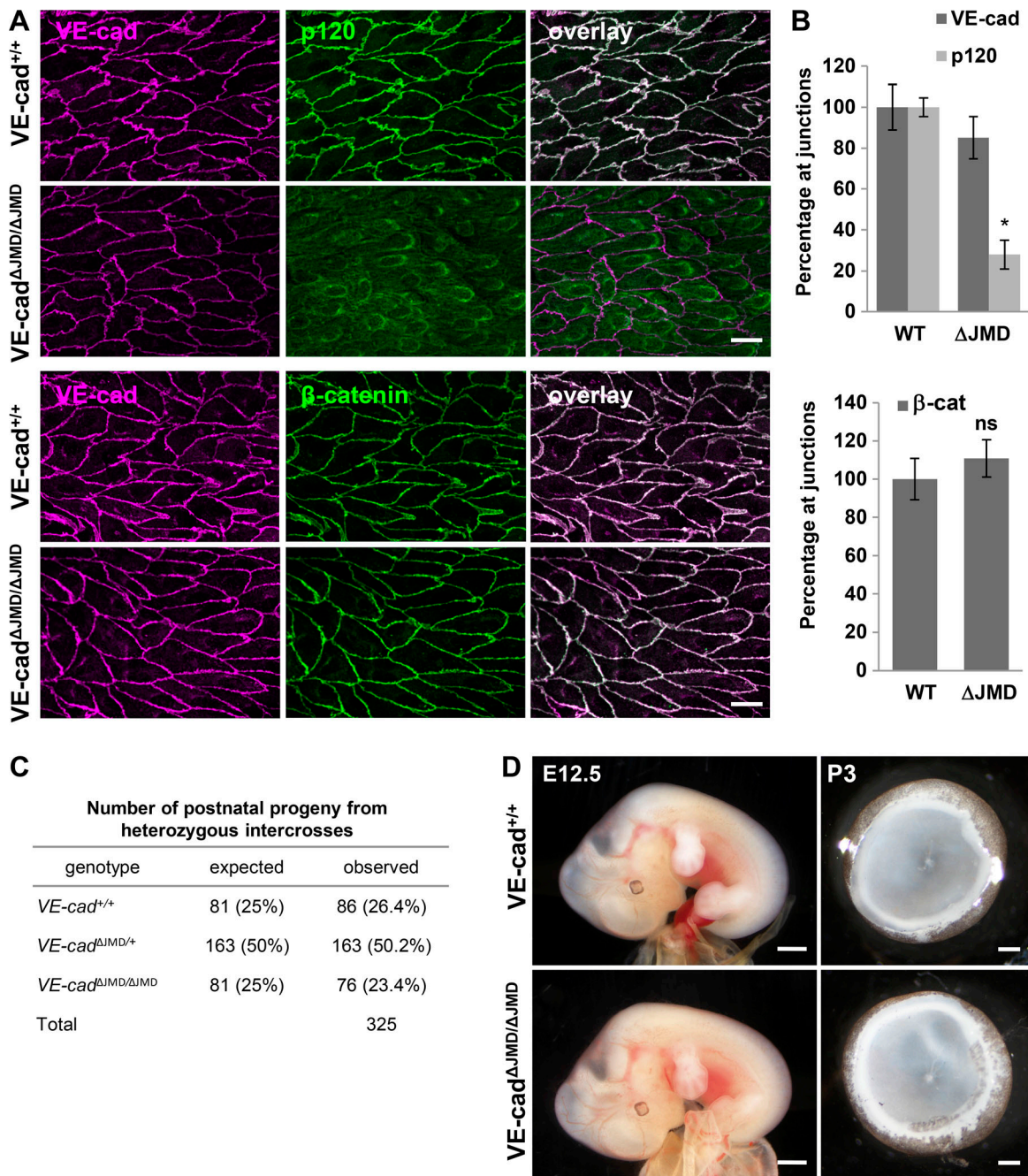


Figure 3. Rescue of VE-cad levels, lethality, and permeability defects in VE-cad Δ JMD endocytic deletion mutant mice. (A) Normal levels of VE-cad at cell borders in VE-cad ^{Δ JMD/ Δ JMD} endocytic mutant mice, despite lack of p120 binding. Aorta en face preparations from VE-cad^{+/+} and VE-cad ^{Δ JMD/ Δ JMD} mice were immunostained for VE-cad (magenta) and p120 (green, top panels) or VE-cad (magenta) and β -catenin (green, bottom panels) and analyzed by confocal microscopy. Normal β -catenin at cell borders was also observed in VE-cad ^{Δ JMD/ Δ JMD} mutants, corresponding to the normal VE-cad levels. Scale bar: 20 μ m. (B) Quantitation of protein levels at cell–cell junctions in the aortas of VE-cad^{+/+} and VE-cad ^{Δ JMD/ Δ JMD} mice. No significant difference was detected in VE-cad or β -catenin levels between VE-cad^{+/+} and VE-cad ^{Δ JMD/ Δ JMD} mice, whereas p120 was significantly decreased at cell junctions. Levels were quantitated from four independent experiments with four to six images per animal and represent the relative mean \pm SEM. *, $P < 0.05$ compared with VE-cad^{+/+}; ns, not significant, Mann–Whitney U test. (C) VE-cad ^{Δ JMD/ Δ JMD} mice from VE-cad ^{Δ JMD/+} intercrosses were born at normal Mendelian ratios and displayed no defects in postnatal survival. The expected number of mice was calculated based on Mendelian genetics. $P = 0.24$ in χ^2 analysis. (D) No increase in hemorrhages in E12.5 whole embryos (left) or P3 eye cups (right) in VE-cad ^{Δ JMD/ Δ JMD} mutant mice compared with VE-cad^{+/+} controls. Scale bar (left): 1 mm; (right): 0.2 mm.

in embryonic lethality associated with decreased VE-cad levels (Oas et al., 2010). Here, we sought to determine if expression of an experimentally stabilized VE-cad could rescue the p120-null phenotype.

To test this possibility, we generated and characterized homozygous VE-cad mutant mice with DEE-to-AAA substitutions (VE-cad^{DEE/DEE}; Fig. 1, A–C). As discussed above, this mutation impairs VE-cad endocytosis in cultured cells (Nanes et al., 2012).

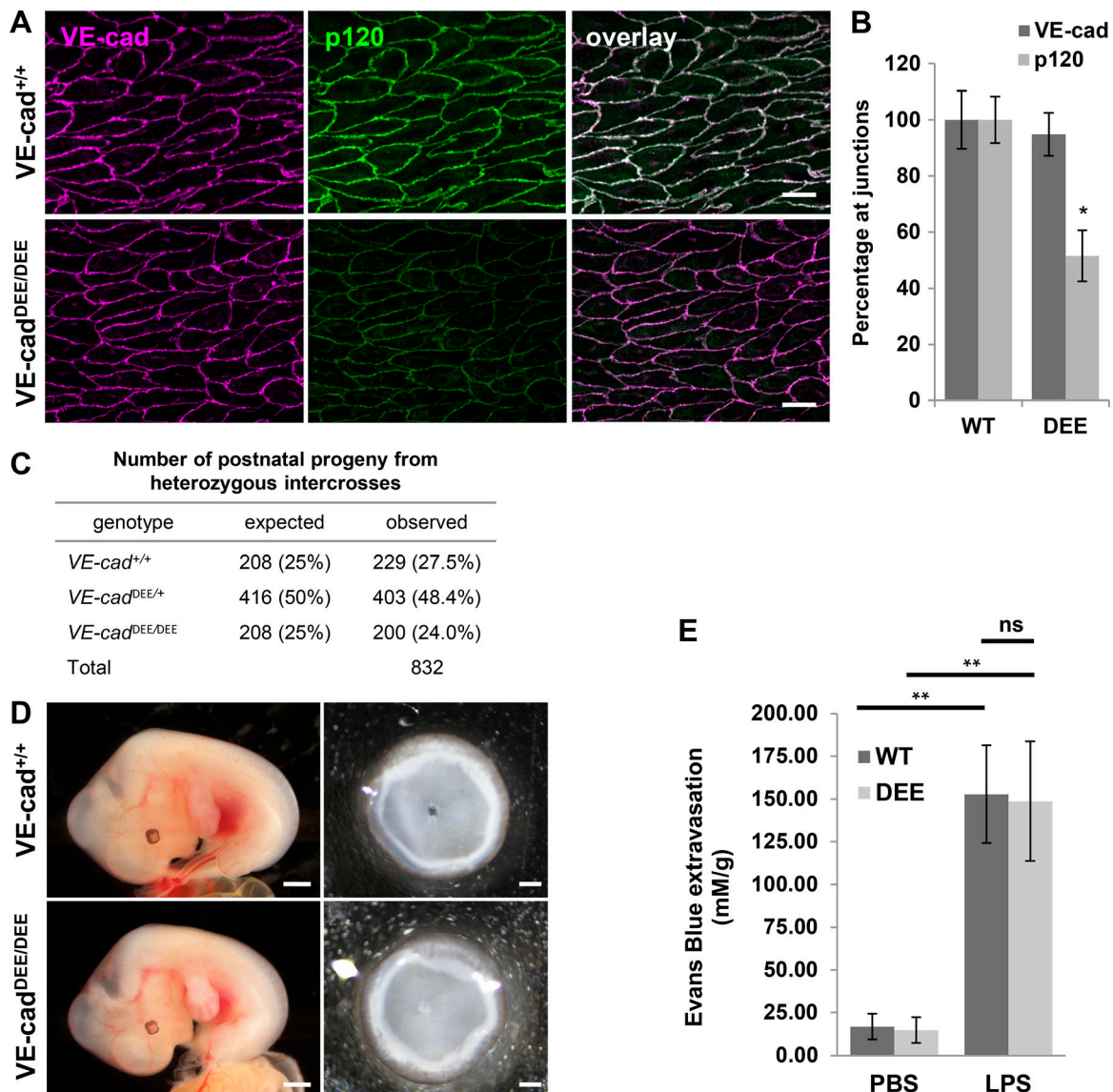


Figure 4. No lethality or permeability defects in DEE endocytic mutant mice. (A) Immunostaining analysis for VE-cad (magenta) and p120 (green) on en face aorta preparations from *VE-cad^{+/+}* and *VE-cad^{DEE/DEE}* adult mice. VE-cad levels at cell junctions appeared normal, whereas p120 levels were partially decreased. Scale bar: 20 μ m. **(B)** Quantitation of VE-cad and p120 levels at cell-cell junctions in the aortas of *VE-cad^{+/+}* and *VE-cad^{DEE/DEE}* mice. Levels were quantitated from five independent experiments with four to six images per animal and are shown as the relative mean \pm SEM. *, $P < 0.05$, Mann-Whitney U test. **(C)** *VE-cad^{DEE/DEE}* mice from *VE-cad^{DEE/+}* intercrosses were born at normal Mendelian ratios and displayed no defects in postnatal survival. $P = 0.49$ in χ^2 analysis. **(D)** Whole embryos at E12.5 (left) and P3 eye cups (right) from *VE-cad^{+/+}* and *VE-cad^{DEE/DEE}* mice. No intraretinal hemorrhaging was observed. Scale bar, left: 1 mm; right: 0.2 mm. **(E)** No increase in vascular permeability in *VE-cad^{DEE/DEE}* mutant mice in response to LPS treatment. Lung permeability was assessed in adult *VE-cad^{+/+}* and *VE-cad^{DEE/DEE}* mice by the Evans blue dye method 6 h after DPBS or LPS treatment. The bar graph represents means \pm SEM with seven mice per group. **, $P < 0.005$; ns, not significant, two-way ANOVA.

We observed significantly decreased levels of p120 at cell borders in the aorta endothelium in these *VE-cad^{DEE/DEE}* mutants (Fig. 4, A and B), consistent with weak binding to p120 (Nanes et al., 2012). Nevertheless, VE-cad levels were normal in *VE-cad^{DEE/DEE}* mutants, with no visible difference compared with WT mice (Fig. 4, A and B). β -Catenin levels at cell junctions were also normal in *VE-cad^{DEE/DEE}* mutants (Fig. S2, B and C). No changes in VE-cad or p120 levels were observed in Western blots of dermal endothelial lysates from these mice (Fig. S1, C and D), and we observed no up-regulation of N-cad in the aorta endothelium (not depicted). Furthermore, we observed expected

Mendelian ratios of homozygous *VE-cad^{DEE/DEE}* mutants 1 wk after birth (24.0%), indicating no lethality in these homozygous mutants (Fig. 4 C). *VE-cad^{DEE/DEE}* mutants also displayed no macroscopic hemorrhaging, either embryonically or postnatally, and displayed no increase in lung permeability in response to LPS challenge (Fig. 4, D and E; and Fig. S2 A). Together, these data suggest that endothelial integrity and barrier function is normal in these mice, similar to *VE-cad ^{Δ JMD/ Δ JMD}* mutants.

The generation of the *VE-cad^{DEE/DEE}* mutant mouse strain allowed us to test the possibility that the p120-null phenotype could be rescued by this stabilized cadherin mutant. We crossed

VE-cad^{DEE/DEE} mutants with p120 conditional knockout mice harboring a p120 floxed allele (Davis and Reynolds, 2006) and used animals expressing Cre recombinase from the Tie2 promoter to delete endothelial p120. Specifically, we mated Tie2-Cre⁺; VE-cad^{DEE/+}; p120^{lox/lox} males to VE-cad^{DEE/+}; p120^{lox/lox} females. Based on normal expected Mendelian ratios, we expected 12.5% of the resulting offspring to be Tie2-Cre⁺; VE-cad^{+/+}; p120^{lox/lox}. However, we observed very few Tie2-Cre⁺; VE-cad^{+/+}; p120^{lox/lox} mice (4 of 156 or 2.6%; Fig. 5 A), consistent with our previous findings that deletion of endothelial p120 is embryonic lethal (Oas et al., 2010). Interestingly, survival was largely rescued in p120-knockout mice expressing a stabilized VE-cad, i.e., Tie2-Cre⁺; VE-cad^{DEE/DEE}; p120^{lox/lox} (19 of 156 or 12.2%; Fig. 5 A). Thus, an experimentally stabilized cadherin rescues the lethality associated with genetic deletion of p120.

The low birth rate of Tie2-Cre⁺; VE-cad^{+/+}; p120^{lox/lox} mice precluded analysis of VE-cad levels in these mice. Therefore, we used the endothelial-specific VE-cad-Cre driver to delete p120 for further analysis. The VE-cad-Cre driver deletes p120 less efficiently than the Tie2-Cre driver, leading to a higher degree of mosaicism and a higher rate of survival of p120 conditional knockout mice. We therefore generated VE-cad-Cre⁺; VE-cad^{+/+}; p120^{lox/lox} (p120^{CKO}; VE-cad^{+/+}) mice and VE-cad-Cre⁺; VE-cad^{DEE/DEE}; p120^{lox/lox} (p120^{CKO}; VE-cad^{DEE/DEE}) mice and analyzed aortic endothelial VE-cad levels in p120⁻ cells. In p120^{CKO}; VE-cad^{+/+} mice, there was a dramatic decrease in VE-cad at borders between p120⁻ cells compared with cells expressing p120 (Fig. 5, B and C). However, in p120^{CKO}; VE-cad^{DEE/DEE} mice, there was virtually no difference in VE-cad levels between p120⁺ and p120⁻ cells (Fig. 5, B and C). Collectively, these results indicate that p120 stabilizes VE-cad in vivo through inhibition of the DEE endocytic signal, and that p120 inhibition of VE-cad endocytosis is the primary endothelial cell function of p120 necessary for survival.

Angiogenesis defects in DEE mutant mice

Endothelial sprouting during angiogenesis is thought to require the modulation of adherens junctions to permit cell intercalations and collective movements during vessel formation (Bentley et al., 2014; Szymborska and Gerhardt, 2018). Cadherin endocytosis has been implicated in the dynamic cell-cell associations required for collective migration, but this possibility has not been tested directly. We hypothesized that blood vessel formation may be altered in VE-cad^{DEE/DEE} mutants owing to decreased VE-cad turnover and decreased junction plasticity. To explore this possibility, we analyzed angiogenesis in the postnatal retinas of VE-cad^{DEE/DEE} mutants. Interestingly, VE-cad^{DEE/DEE} mutants exhibited a decrease in vascular density and total length of vessels, as well as decreased vessel branching (Fig. 6, A and B). However, we did not observe an increase in blind-ending vessels in the mutant, indicating that the angiogenesis defects were due to failures in initial endothelial sprout formation rather than vessel stabilization (Fig. 6 A and not depicted).

To further investigate vascular defects in the VE-cad^{DEE/DEE} mutant, we analyzed blood vessel organization in the developing yolk sac. Following formation of the primitive vascular plexus

(E8.5), vessels undergo extensive angiogenic remodeling events that involve nascent vessel sprouting, intussusception, vessel fusion, and pruning, leading to a hierarchically ordered network of branched vessels visible by E9.5 (Garcia and Larina, 2014; Udan et al., 2013). Examination of yolk sac whole-mount preparations from the VE-cad^{DEE/DEE} mutants revealed normal formation of vitelline and larger-diameter vessels, but abnormal microvascular patterning (Fig. 6 C). In particular, many microvessels were enlarged and appeared to have undergone less angiogenic remodeling than in WT littermates. Quantitation revealed a slight increase in vascular density in the mutants compared with their WT littermates, as well as a significant decrease in the total vessel length and branching (Fig. 6 D). Thus, vessels are dilated and the network is less complex in the VE-cad^{DEE/DEE} mutants compared with WT littermates. To further test for the presence of sprouting defects in VE-cad^{DEE/DEE} mutants, we performed ex vivo aortic ring assays. Rings cut from adult aortas were embedded in Matrigel, and the area of sprout outgrowth was quantified after 5 or 7 d of growth. As shown in Fig. 6 (E and F), VE-cad^{DEE/DEE} mutants exhibited significantly reduced network formation at both time points compared with WT littermate controls. Together, these data reveal an essential role for VE-cad endocytosis for endothelial remodeling and sprouting angiogenesis.

VE-cad endocytosis is required for endothelial polarization and collective cell migration

Sprouting angiogenesis is a form of collective cell movement involving dynamic and continuous interchange between endothelial cells migrating as groups, driven in part by differential adhesion (Bentley et al., 2014). We hypothesized that reduced junction plasticity could inhibit collective migration, which in turn could lead to the observed vessel patterning defects. To test this, we isolated primary endothelial cells from the dermis of early postnatal WT and VE-cad^{DEE/DEE} pups and performed scratch wound migration assays. Analysis of wound closure over a 12-h period revealed a slower migration rate of VE-cad^{DEE/DEE} endothelial cells compared with WT endothelial cells (Fig. 7, A and B). We observed no migration defects in VE-cad^{GGG/GGG} mutant endothelial cells, consistent with normal microvessel development observed in these mutant mice (Fig. S3, A and B). Together, these data indicate that VE-cad endocytosis is required for the collective cell movements that occur during sprouting angiogenesis.

Polarization of the cell motility machinery is a critical first step during collective cell migration. This polarization involves asymmetric membrane trafficking, centrosome/Golgi complex reorientation toward the leading edge, polarized activation of Rho family GTPases, and remodeling of the microtubule and actin cytoskeletons to generate a protrusive front and a retracting rear (Khalil and de Rooij, 2019; Mayor and Etienne-Manneville, 2016). To investigate whether VE-cad endocytosis is required for polarization during collective migration, we examined reorientation of the Golgi apparatus in VE-cad^{DEE/DEE} mutant endothelial cells in response to wounding. Primary WT or VE-cad^{DEE/DEE} mutant endothelial cells were processed for immunofluorescence localization of VE-cad and the Golgi

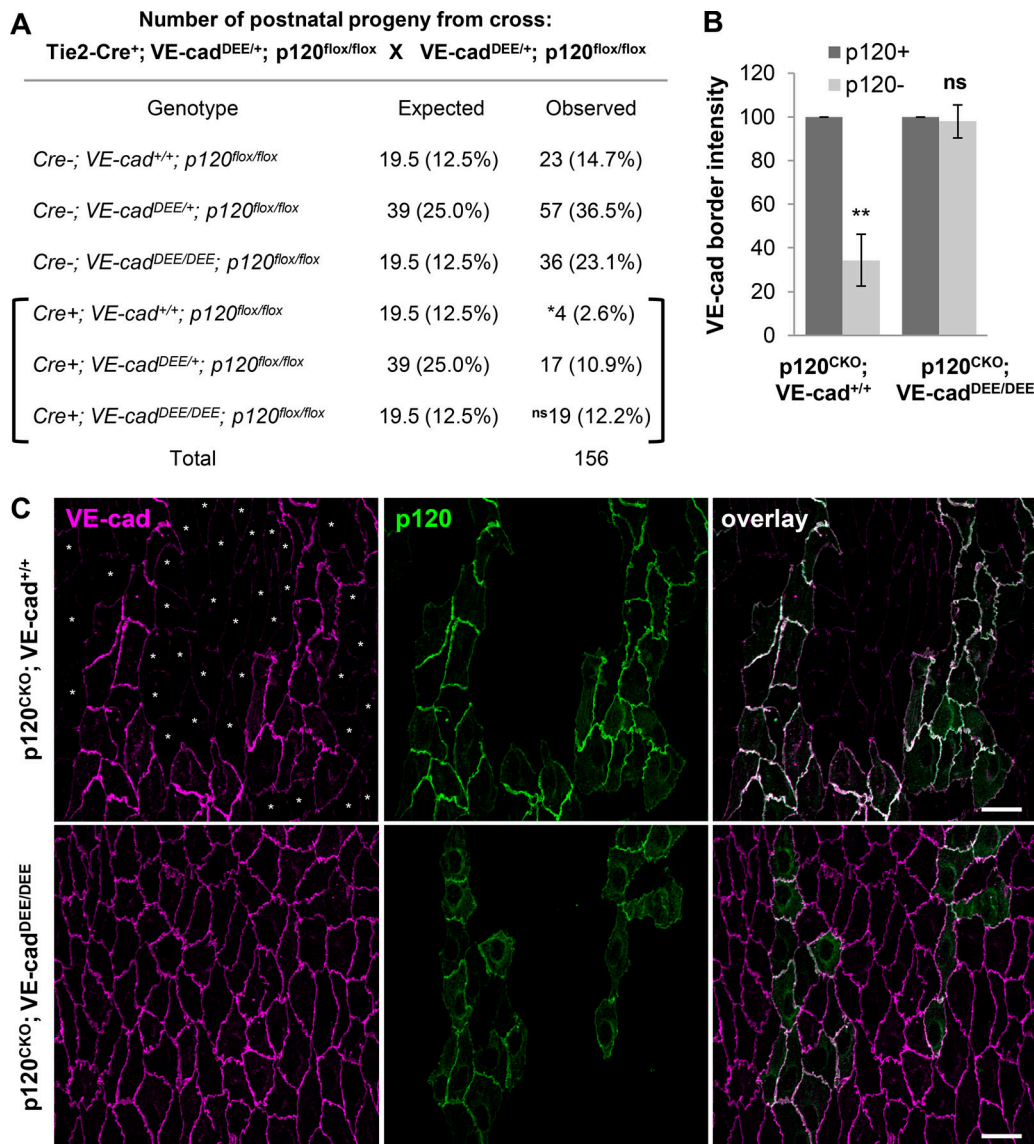


Figure 5. Rescue of VE-cad levels and lethality in p120 conditional knockout mice with mutation of VE-cad endocytic motif. (A) Genotyping analysis of postnatal offspring from Tie2-Cre⁺; VE-cad^{DEE/+}; p120^{fl/fl} × VE-cad^{DEE/+}; p120^{fl/fl} matings. Less than expected numbers of Tie2-Cre⁺; VE-cad^{+/+}; p120^{fl/fl} mice were born, based on expected Mendelian ratios, suggesting significant perinatal lethality in the presence of WT VE-cad. However, Tie2-Cre⁺; VE-cad^{DEE/DEE}; p120^{fl/fl} mice were born near expected ratios, suggesting a rescue of lethality with disruption of the VE-cad endocytic motif. Genotyping was performed between P6 and P8, and the expected number of mice was based on the total number of mice and Mendelian genetics. *, $P < 0.05$; ns, not significant in χ^2 analysis. **(B)** Quantitation of VE-cad levels at cell borders between adjacent p120⁺ or adjacent p120⁻ cells in the aortas of VE-cad-Cre⁺; p120^{fl/fl}; VE-cad^{+/+} (p120^{CKO}; VE-cad^{+/+}) and VE-cad-Cre⁺; p120^{fl/fl}; VE-cad^{DEE/DEE} (p120^{CKO}; VE-cad^{DEE/DEE}) mice as shown in C. VE-cad levels at p120⁺ cell borders were set to 100 and the percentage decrease in p120⁻ cells was quantitated. Graph represents the relative mean \pm SEM, calculated from three mice per genotype, with 5–10 fields of view from each mouse and ≥ 10 p120⁺ and p120⁻ borders per field; **, $P < 0.005$ compared with p120⁺; ns, not significant, t test. **(C)** Rescue of VE-cad levels in p120-null cells by mutation of the DEE endocytic motif. Aorta en face immunostaining of p120^{CKO}; VE-cad^{+/+} (top panels) or p120^{CKO}; VE-cad^{DEE/DEE} mice (bottom panels). Mosaic Cre-mediated deletion of p120 led to both p120⁺ (green) and p120⁻ cells within the same field of view. In p120^{CKO}; VE-cad^{+/+} mice, VE-cad (magenta) levels were significantly decreased in p120⁻ cells (asterisk), suggesting that p120 is required for VE-cad membrane stability. In p120^{CKO}; VE-cad^{DEE/DEE} mice, no decrease in VE-cad levels were observed in p120⁻ cells, suggesting that disruption of the DEE endocytic signal can stabilize VE-cad membrane levels in the absence of p120 binding. Scale bar: 25 μ m.

marker, GM-130, together with DAPI at various times after wounding. We defined cells with the Golgi localized within a 90° quadrant between the nuclei and the wound edge as polarized cells (see drawing in Fig. 7 D). As shown in Fig. 7, C and D, we observed a slower rate of polarization of the VE-cad^{DEE/DEE} mutant endothelial cells compared with WT cells in response to wounding. After 2 h, 62% of WT cells were polarized, whereas

only 45% of DEE mutant cells were polarized. Likewise, 75% of WT cells were polarized after 4 h, whereas only 52% of mutant cells were polarized. At 6 h, although the percentage of DEE mutant cells was still slightly decreased compared with WT, this difference was no longer statistically significant. Thus, VE-cad^{DEE/DEE} mutant cells eventually polarize, but at a slower rate than WT cells. We observed similar Golgi reorientation

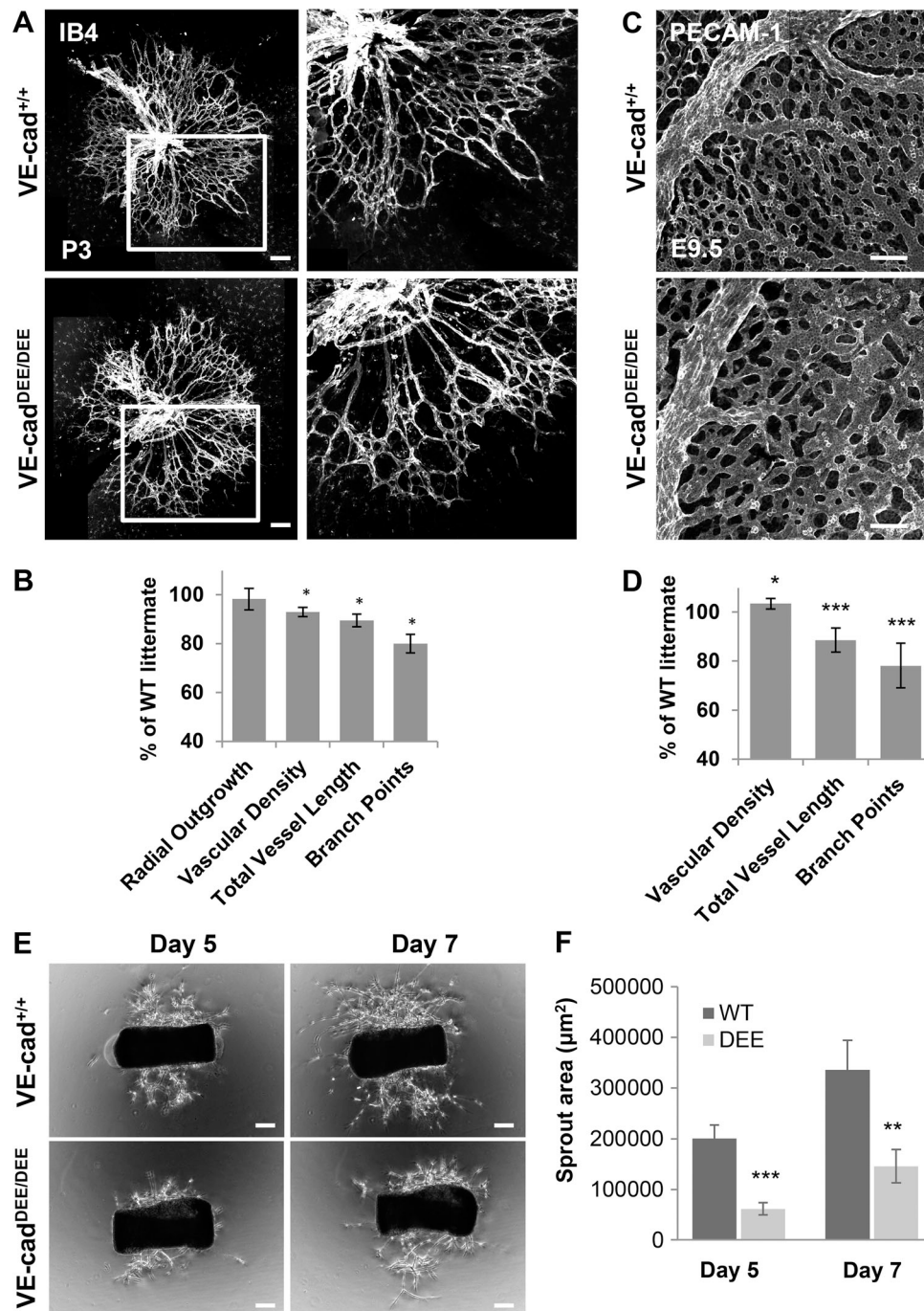


Figure 6. Defects in blood vessel morphology in VE-cad DEE endocytic mutant mice. (A) Decreased angiogenesis in VE-cad^{DEE/DEE} mutant retinas at P3, as revealed with isolectin-B4 staining. VE-cad^{DEE/DEE} mutants displayed decreased vessel density and branching at the vessel front compared with VE-cad^{+/+} littermates. Panels on the right show higher magnification of the boxed region in left panels. Scale bar: 100 μm. **(B)** Quantitation of the vascular parameters per unit area at the vessel front in P3 VE-cad^{DEE/DEE} retinas. Data are presented as percentage of WT littermate control, and graph represents mean ± SEM; n = 6 independent litters. *, P < 0.05, paired t test. **(C)** Decreased blood vessel formation in VE-cad^{DEE/DEE} mutant yolk sacs at E9.5. Yolk sacs were immunostained for PECAM-1 to visualize blood vessels. Scale bar: 100 μm. **(D)** Quantitation of vascular morphology in VE-cad^{DEE/DEE} mutant yolk sacs at E9.5. Data are presented as percentage of WT littermate control. *, P < 0.01; ***, P < 0.0001, t test; n = 25 images from five separate litters. **(E)** Decreased vessel outgrowth in ex vivo aortic ring assays in VE-cad^{DEE/DEE} mutant mice. 1-mm rings from the aortas of adult VE-cad^{+/+} or VE-cad^{DEE/DEE} mice were embedded in Matrigel and analyzed after 5 and 7 d for vessel outgrowth by phase contrast. Scale bar: 150 μm. **(F)** Area of vessel outgrowth from aortic rings at the indicated days was quantitated. Graph shows the relative mean ± SEM, calculated from n = 10–12 rings per genotype, and is representative of four independent experiments. **, P < 0.01; ***, P < 0.001, t test.

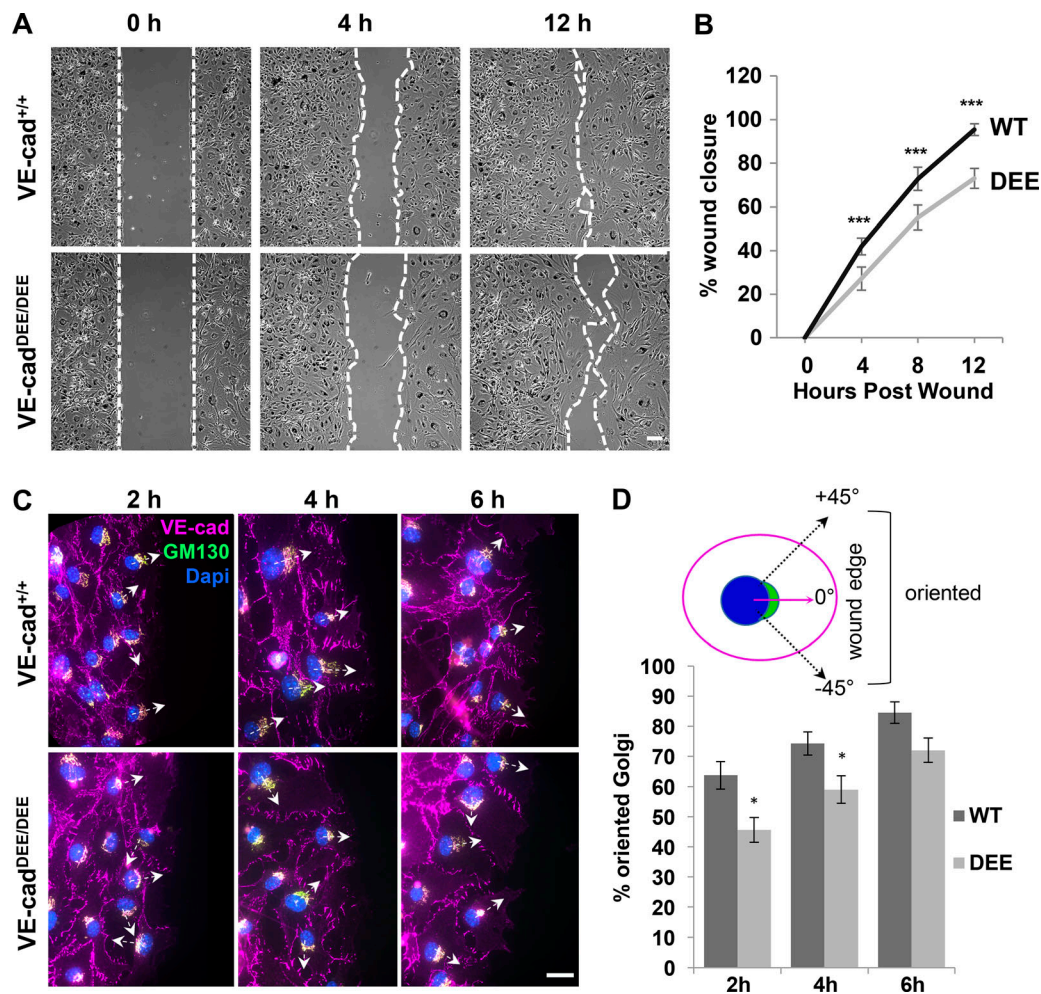


Figure 7. VE-cad DEE endocytic motif is required for endothelial migration and polarization in vitro (A) Decreased migration of isolated VE-cad^{DEE/DEE} mutant dermal endothelial cells in vitro. Scratch-wound assays were performed with primary dermal MECs isolated from VE-cad^{+/+} and VE-cad^{DEE/DEE} mutant mice. White dashed lines denote scratch borders. Scale bar: 100 μ m. **(B)** The percentage wound closure by VE-cad^{+/+} and VE-cad^{DEE/DEE} mutant cells was calculated over 12 h using phase-contrast microscopy. Graph shows the relative mean \pm SD and is representative of four independent experiments. ***, $P < 0.001$, t test, $n = 8$ images per genotype. **(C)** Decreased polarization in wound-edge VE-cad^{DEE/DEE} mutant endothelial cells at the indicated time points after wounding. Golgi polarity in wound edge cells was analyzed by immunostaining for the Golgi marker GM-130 (green), nuclei (blue), and VE-cad (magenta). Arrows indicate the nucleus-Golgi polarity axis. Scale bar: 25 μ m. **(D)** The percentage of cells with their Golgi polarized toward the wound edge in scratch wound assays was determined at 2, 4, and 6 h after wounding. A line from the nucleus through the center of the Golgi was drawn, and the percentage of cells correctly oriented at $\pm 45^\circ$ toward the wound edge was calculated. At least 100 cells were analyzed for each genotype for each time point. Graph is representative of four independent experiments. *, $P < 0.05$, two-proportion Z test.

defects in wounded human microvascular endothelial cells (MECs) expressing the VE-cad DEE \rightarrow AAA (VE-cadDEE) mutant, but not those expressing WT VE-cad or the GGG \rightarrow AAA (VE-cadGGG) mutant (Fig. S3, C and D). These findings suggest that cadherin-mediated polarization does not require p120 binding. These data also suggest that the VE-cadDEE mutant can act dominantly over WT to suppress polarization. Thus, stabilization of VE-cad on the cell surface inhibits the ability of endothelial cells to polarize in response to directional migration cues.

VE-cad endocytosis permits actin cytoskeleton reorganization during endothelial polarization

Cadherin-mediated adhesions have previously been shown to regulate cell polarity in wounded monolayers and cell colonies in an actin cytoskeleton-dependent manner (Desai et al., 2009;

Dupin et al., 2009). Moreover, remodeling of the actin cytoskeleton is known to play a crucial role in the collective migration of endothelial cells and in the reorganization of endothelial cell junctions (Huvneers and de Rooij, 2013; Vitorino and Meyer, 2008). We hypothesized that expression of the stabilized VE-cadDEE mutant, which interacts with the actin cytoskeleton through C-terminal β -catenin binding (Nanes et al., 2012), may be inhibiting reorganization of the actin cytoskeleton in wound edge cells and thereby preventing polarization. Previous studies have shown that more mature, stable junctions are associated with parallel actin bundles that form a broad band around the cell periphery (Huvneers et al., 2012; Zhang et al., 2005). However, collective cell movements induced by scratch wounding lead to a reduction in junctional actin and the formation of new radial actin bundles (de Rooij et al., 2005;

Huveneers and de Rooij, 2013; le Duc et al., 2010; Mangold et al., 2011). Therefore, we examined this reorganization of the actin cytoskeleton in wounded human umbilical vein endothelial cells (HUVECs) expressing either VE-cadWT or VE-cadDEE. 1 h after wounding, we found that both VE-cadWT and VE-cadDEE cells at the wound edge displayed a mix of thick cortical actin bundles and/or thin radial actin bundles (Fig. 8 A). However, VE-cadDEE mutant cells showed an increased number of thick peripheral actin bundles that oriented parallel to the junctions and a decreased number of radial actin filaments (Fig. 8 A). Live-cell imaging revealed that these thick, cortical actin bundles were very stable in the VEcadDEE mutant cells and would often persist throughout the 2-h imaging time course (Fig. S4). To quantify these defects in actin reorganization, we wounded cells and stained for F-actin 1 h after wounding. We did not detect any difference between the overall mean fluorescence intensity of F-actin in VE-cadWT- and VE-cadDEE-expressing cells, suggesting that the total cellular levels of F-actin are unaffected (Fig. 8 B). However, when we applied a threshold mask to the F-actin staining and measured the threshold area within individual wound-edge cells, we did detect a significant reduction in the threshold area of VE-cadDEE-expressing cells (Fig. 8 C). This observation suggests that actin filaments are organized predominantly in thick cortical bundles in the VE-cadDEE cells compared with VE-cadWT.

Previous studies demonstrated that cadherin is internalized from cell-cell borders at the rear of migrating wound edge cells (Peglion et al., 2014). Consistent with these previous observations, we frequently observed endocytic vesicles budding from the rear cell-cell contacts of wound edge endothelial cells (Fig. S4). These endocytic events were reduced by ~44% in cells expressing the VE-cadDEE mutant compared with VE-cad WT. These data suggest that VE-cad endocytosis might be required for reorganization of the actin cytoskeleton in response to wounding. If this model is correct, VE-cadDEE-induced polarization defects should be rescued by temporarily disrupting the connection between actin and VE-cad. To test this possibility, we wounded cells and then immediately treated them with the actin depolymerizing drug Cytochalasin D (CytoD) for 2 h, followed by a 3-h washout in normal growth medium. Immediately following CytoD treatment, no actin filaments were visible in either VE-cadWT or VE-cadDEE mutant cells (Figs. 8 D and S5). Instead, only a few clumps of F-actin were present at the cell membrane. VE-cad localization was also affected, appearing more patchy and less uniformly distributed than starved but untreated cells. Washout of CytoD led to the rapid recovery of the actin cytoskeleton. 1 h after washout, prominent actin filaments were observed, and VE-cad at cell-cell borders appeared normal in both VE-cadWT and VE-cadDEE cells (Fig. S5). 3 h after washout, a mix of thick cortical actin bundles and thin radial actin filaments could be found in both VE-cadWT and VE-cadDEE cells (Figs. 8 D and S5). This finding suggests that the CytoD treatment relieved the block on actin remodeling in VE-cadDEE mutant cells. Interestingly, the Golgi polarization defects in VE-cadDEE mutant cells were also rescued following CytoD treatment and washout (Fig. 8, E and F). Together, these data suggest that VE-cad endocytosis controls polarization by

promoting reorganization of the actin cytoskeleton during collective migration.

The data above suggest that VE-cad endocytosis is coordinated with actin remodeling through VE-cad connections to the actin cytoskeleton. To test this possibility further, we generated a VE-cad Δ CBD-DEE compound mutant. This mutant contains both the DEE mutation and a deletion of the C-terminal CBD, thereby uncoupling the endocytic mutant from the actin cytoskeleton. Similar to the experiments above, we analyzed Golgi reorientation in VE-cad Δ CBD-DEE-expressing cells. Interestingly, cells expressing the VE-cad Δ CBD-DEE compound mutant exhibited normal polarization after wounding (Fig. 8, G and H). 2 h after wounding, $60.3 \pm 4.4\%$ of VE-cad Δ CBD-DEE-expressing cells were polarized, whereas only $37.5 \pm 4.9\%$ of VE-cadDEE mutant cells were polarized. Together, these data suggest that cadherin endocytosis is required for changes in actin organization that promote polarization during collective migration. Furthermore, these findings indicate that the functions of the p120 and CBDs of the cadherin tail are integrated to modulate cell polarity and directional movement.

Discussion

The findings presented here advance two important aspects of classic cadherin biology. First, although p120 participates in numerous cellular activities, we used multiple experimental approaches to demonstrate that the primary function of p120 is to stabilize cell-surface cadherin. Indeed, mice harboring a VE-cad mutant (VE-cad Δ JMD/ Δ JMD) unable to bind p120 but lacking the DEE endocytic motif are apparently normal, even though endothelial cells in these animals lack junctional p120. Similarly, the lethality of the endothelial p120-null phenotype can be largely rescued by expressing a VE-cad mutant deficient in endocytic activity (VE-cad $^{DEE/DEE}$). Thus, p120 can be rendered dispensable in the context of a stabilized cadherin. Second, we used the VE-cad $^{DEE/DEE}$ endocytic mutant to reveal that cadherin endocytosis is required for normal tissue morphogenesis. Surprisingly, VE-cad endocytosis regulates endothelial migration by permitting cell polarization at the onset of collective cell migration. Thus, the cadherin-p120 complex dictates the plasticity of endothelial junctions to govern key functions of vascular endothelial cells, including endothelial cell migration, microvascular patterning, and acquisition of the vascular barrier.

Previous studies in *Drosophila* indicate that p120 is not required for survival (Myster et al., 2003; Pacquelet et al., 2003). Subsequent to these initial studies in flies, a series of p120 conditional null mouse mutants confirmed that p120 is essential for cadherin function in most vertebrate tissues, including vascular endothelial cells (Cadwell et al., 2016; Oas et al., 2010). However, these previous vertebrate studies do not determine if p120 is required at the cadherin complex or if p120 is performing other essential functions independent of cadherin binding. Our analysis of the VE-cad $^{GGG/GGG}$ mutant in Fig. 1 demonstrates that p120 binding to the cadherin tail is critical for cadherin stability in vivo in a vertebrate model system. Although p120 was still present at normal levels in VE-cad $^{GGG/GGG}$ mutant endothelial cells, it failed to localize to cell junctions. VE-cad levels were

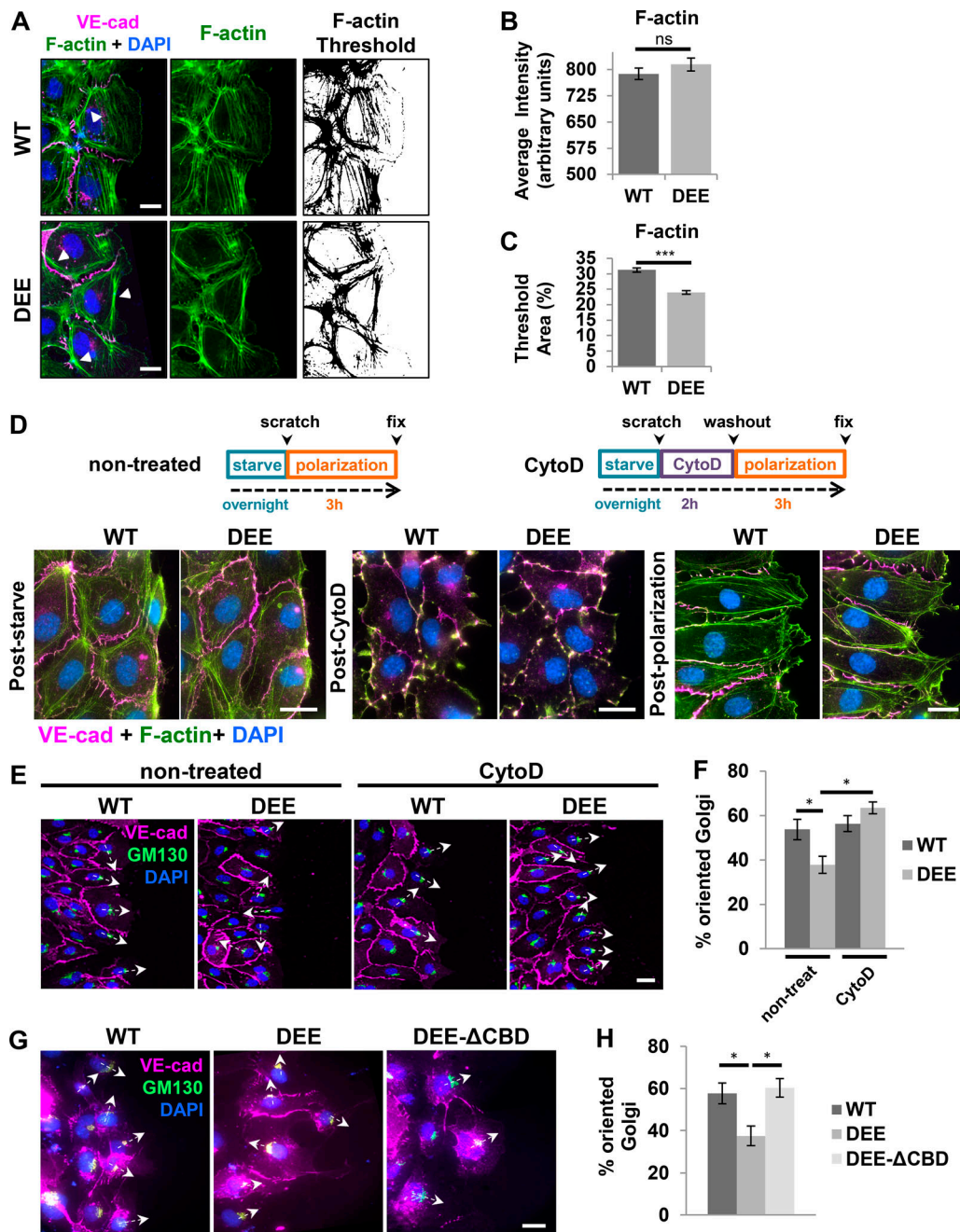


Figure 8. Endothelial polarization driven by VE-cad endocytosis requires actin reorganization. (A) Representative images show a wounded monolayer of HUVECs transfected with either VE-cadWT-RFP or VE-cadDEE-RFP (magenta) and stained with DAPI (blue) and phalloidin-488 (green) to show F-actin. VE-cadDEE-RFP mutant cells display a reduction in radial actin filaments and an increase in cortical F-actin bundles (arrowheads). Panels on the right are binary images showing the threshold applied to identify F-actin. Scale bar: 15 μ m. (B) Quantitation of the mean F-actin (phalloidin-488) fluorescence intensity of VE-cadWT-RFP- and VE-cadDEE-RFP-expressing cells. Graph represents mean \pm SEM calculated from three independent experiments, with ≥ 50 cells per experiment; ns, not significant, *t* test. (C) Quantitation of the mean F-actin threshold area. A manual threshold was applied to the phalloidin-488 image to identify all actin-positive areas within individual wound edge cells. Data are presented as the percentage of individual cell area that was thresholded. Graph represents mean \pm SEM calculated from three independent experiments, with ≥ 50 cells per experiment. ***, $P < 0.0001$, *t* test. (D) Top panels show experimental design. Cells were transfected with RFP-tagged VE-cadWT or VE-cadDEE adenovirus and then starved overnight. The next morning, cells were wounded and then either incubated for 2 h with 1 μ M CytoD followed by 3 h washout (CytoD) or left untreated for 3 h following wounding (nontreated). Cells were then fixed and immunostained for RFP (magenta), together with DAPI (blue) and phalloidin-488 (green) to visualize the actin cytoskeleton. See Fig. S5 for individual channels. Scale bar: 20 μ m. (E) Rescue of Golgi reorientation defects in VE-cadDEE-expressing cells after CytoD treatment and washout. Transduced cells were starved, wounded, and either treated with CytoD or left untreated as described in D. Cells were then fixed and immunostained for RFP (magenta), GM-130 (green), and nuclei (blue) to visualize reorientation of the Golgi toward the wound edge. Arrows indicate the nucleus-Golgi polarity axis. Scale bar: 25 μ m. (F) Graph shows the average percentage \pm SEM of RFP-positive cells with a polarized Golgi apparatus (in a 90° quadrant toward the wound edge) 3 h after washout (treated) or wounding (untreated). Graph represents average \pm SEM calculated from four independent experiments. At least 80 cells were analyzed per condition. *, $P < 0.05$, one-way ANOVA with Tukey post hoc test. (G) Rescue of polarization defects in VE-cadDEE-expressing cells by deletion of the CBD. HUVEC endothelial

cells were transduced with lentivirus coding for the indicated RFP-tagged VE-cad proteins. Cells were fixed 2 h after wounding and immunostained for GM-130 (green) and nuclei (blue) to visualize reorientation of the Golgi toward the wound edge. The RFP signal is shown in magenta. Arrows indicate the nucleus-Golgi polarity axis. Scale bar: 20 μm . **(H)** Graph shows the average percentage of RFP-positive cells with their Golgi apparatus polarized in a 90° quadrant toward the wound edge 2 h after wounding. At least 60 cells were analyzed per condition. Graph represents average \pm SEM calculated from three independent experiments. *, $P < 0.05$, one-way ANOVA with Tukey post hoc test.

reduced in these animals, and vessel stability was compromised, as demonstrated by the presence of embryonic and postnatal hemorrhaging. In addition, these animals were highly susceptible to challenges to the vascular barrier and displayed large increases in lung permeability in response to LPS treatment. Thus, in this vertebrate model system, p120 binding to cadherin is required for normal cadherin expression levels, adherens junction integrity, and overall viability.

Our previous studies demonstrated that the core p120 binding domain of VE-cad harbors a 3-aa endocytic signal (DEE; Nanes et al., 2012). We hypothesized that cadherin JMD deletions that eliminated both p120 binding and the DEE endocytic motif would result in a cadherin that is deficient in p120 binding but simultaneously stable at the cell surface. Using the CRISPR-Cas system, we generated animals with an 11-aa deletion that completely eliminated p120 binding and the DEE endocytic motif (VE-cad ^{Δ JMD/ Δ JMD}). In Fig. 3, analysis of junctional p120 in aortic endothelial cells of this mutant revealed that p120 was completely absent from junctions, while VE-cad levels were identical to WT controls. Remarkably, these animals were viable and lacked the hemorrhaging and runting phenotypes associated with the VE-cad^{GGG/GGG} mutation. These results indicate that a classic cadherin can be rendered p120 independent by cadherin mutations that eliminate endocytic activity.

To further examine the requirement for p120, we tested whether a VE-cad endocytic mutant (VE-cad^{DEE/DEE}) could rescue the endothelial p120-null phenotype. Indeed, most p120-null animals expressing the VE-cad^{DEE/DEE} mutation survived, in contrast to animals expressing WT VE-cad, which exhibited almost complete embryonic lethality (Fig. 5). Furthermore, VE-cad levels at cell-cell borders in VE-cad^{DEE/DEE} mutants lacking p120 were normal, confirming that the VE-cad^{DEE/DEE} mutant is stable in the absence of p120 binding. However, it should be noted that often the surviving Tie2-Cre; VE-cad^{DEE/DEE}; p120^{flox/flox} mice were smaller than their Cre-negative littermates, and occasionally died within a few weeks after weaning. There are at least two possible explanations for this outcome. One likely possibility is that p120 is also required for N-cad regulation. N-cad levels are reduced in endothelial cells lacking p120 (Davis et al., 2003; Ferreri et al., 2008; Oas et al., 2010), and several studies indicate that N-cad is essential for early vascular development and pericyte recruitment (Luo and Radice, 2005; Tillet et al., 2005). Second, p120 is known to perform other, cadherin-independent functions such as the regulation of Rho GTPases and Kaiso-mediated transcriptional regulation (Anastasiadis, 2007; Anastasiadis et al., 2000; Anastasiadis and Reynolds, 2001; Duñach et al., 2017; Kourtidis et al., 2013). Thus, the complete loss of p120 is likely to be more severe than the VE-cad^{GGG/GGG} mutation, because multiple cadherins are affected by loss of p120 and because p120 carries

out cadherin-independent roles. Likewise, it is possible that VE-cad^{DEE/DEE} mutants lacking endothelial p120 also possess other significant, but as of yet uncharacterized, vascular defects that reflect cadherin-independent roles for p120 in vascular endothelial cell function.

Several studies have reported that abrogation of VE-cad expression leads to vessel hypersprouting in mice (Gaengel et al., 2012) and zebrafish (Abraham et al., 2009; Montero-Balaguer et al., 2009). However, we did not observe an aberrant patterning or sprouting phenotype in VE-cad^{GGG/GGG} mutants. Although blood spots were increased by fivefold in the VE-cad^{GGG/GGG} mutant retina, blood vessel density and patterning were similar to those of WT. One possibility is that endothelial cells need a threshold level of VE-cad to prevent excess sprouting. This idea is supported by a VE-cad knockdown study in zebrafish (Montero-Balaguer et al., 2009). Although high concentrations of VE-cad morpholinos prevented the establishment of reciprocal contacts between vessels, leading to increased sprouting, low doses of VE-cad morpholinos led to vascular fragility, hemorrhages, and increased permeability, a phenotype reminiscent of VE-cad^{GGG/GGG} mutants. Therefore, the mechanisms by which VE-cad controls sprouting behavior are likely complex and dependent on the levels of VE-cad present.

It is interesting to note that the severity of the vascular integrity phenotype in various VE-cad mutants directly correlates with the levels of VE-cad present at cell junctions. In homozygous null mice, a complete lack of VE-cad leads to severe vascular defects and early embryonic death due to the regression and disintegration of nascent blood vessels (Carmeliet et al., 1999; Crosby et al., 2005; Gory-Fauré et al., 1999). However, heterozygous null mice, which display a 50% reduction in VE-cad levels, were reported to have no obvious defects (Carmeliet et al., 1999; Gory-Fauré et al., 1999). The VE-cad^{GGG/GGG} mutants reported here display a 70% reduction in VE-cad levels and have a moderately severe phenotype (Fig. 1). The VE-cad ^{Δ JMD/ Δ JMD} and VE-cad^{DEE/DEE} mutants have normal VE-cad levels and no hemorrhaging or lethality. We would therefore predict that any further reduction of functional VE-cad in VE-cad^{GGG/GGG} mutants would lead to a more severe phenotype. Consistent with this possibility, we found that VE-cad^{GGG/STOP} mutants all die embryonically. Together, these data suggest that a threshold level of VE-cad between 30 and 50% of normal levels is required for normal vascular integrity and survival.

It is also interesting to note that the VE-cad^{GGG/GGG} mutants that survived the first few postnatal days usually survived into adulthood. We did not observe an increase in the death rate of older (P7 or later) VE-cad^{GGG/GGG} mutants, despite their having reduced VE-cad levels. Furthermore, the reduced body weight of VE-cad^{GGG/GGG} mutants was more pronounced at 3 wk compared with 6 wk (Fig. 1). Together, this suggests that the maintenance

of normal VE-cad levels is most critical during the early stages of blood vessel morphogenesis, and that other mechanisms likely compensate for reduced VE-cad levels during later developmental stages. It is unlikely that N-cad was compensating for the loss of VE-cad in VE-cad^{GGG/GGG} mutants, because we failed to observe N-cad at cell junctions in the mutant aortas. In addition, β -catenin levels at cell junctions paralleled the reduction of VE-cad at junctions. Thus, once the adherens junctions are formed, they can likely be maintained despite loss of cadherin. This finding is supported by work from Frye et al. (2015) showing that induced deletion of the VE-cad gene in adult (7-wk-old) mice led to increased vascular permeability in the heart and lungs but no obvious vascular abnormalities or lethality.

A previous study showed that expression of the VE-cad^{DEE} endocytic mutant could inhibit angiogenesis in fibrin beads assays *in vitro* (Garrett et al., 2017). Furthermore, a number of studies have implicated cadherin endocytosis in the regulation of tissue morphogenesis in both flies and mice. However, a limitation of previous studies is the reliance on broad inhibition of endocytic or recycling pathways to modulate cadherin trafficking (Cadwell et al., 2016; Ratheesh and Yap, 2010). The generation of the VE-cad^{DEE/DEE} mouse line allowed us to directly test the role of cadherin endocytosis in vertebrate morphogenesis. The formation of large vessels was grossly normal in these mutants. However, as shown in Fig. 6, VE-cad^{DEE/DEE} mutants displayed defects in vessel density, length, and branching during postnatal retina angiogenesis. These mutants also exhibited decreased vessel length and branching in the yolk sac microvasculature, as well as less neovessel outgrowth in *ex vivo* aortic rings. Endothelial cells isolated from the VE-cad^{DEE/DEE} mutant mice were defective in collective migration, as assessed using scratch wound assays (Fig. 7). Similar collective cell migration defects were observed in MECs expressing the VE-cad^{DEE} mutant but not in cells expressing WT VE-cad or the VE-cad^{GGG} mutant. It is interesting to note that we observed no increase in VE-cad levels in the VE-cad^{DEE/DEE} mutant, either *in vitro* or *in vivo*. This finding suggests that cells use unknown mechanisms to limit total cadherin cell-surface levels when turnover rates are experimentally reduced. Furthermore, our results suggest that VE-cad endocytic rates rather than overall cadherin expression levels are the critical determinant controlling collective migration.

Analysis of migratory activity of cells expressing the VE-cad^{DEE/DEE} mutant revealed that VE-cad endocytosis is required for endothelial cell polarization at the onset of collective cell migration. This defect was observed both in cells isolated from VE-cad^{DEE/DEE} mutant mice and in endothelial cells exogenously expressing the VE-cad^{DEE} mutant. Importantly, deletion of the CBD from the tail of the VE-cad^{DEE} mutant relieved these polarity and migration defects caused by the endocytic mutation, as shown in Fig. 8. Furthermore, disruption of the actin cytoskeleton, using CytoD followed by washout, rescued the polarity defects in cells expressing the VE-cad^{DEE} mutant. Together, these data indicate that linkage to the actin cytoskeleton is required for the inhibitory activity of the DEE mutant. We also observed altered organization of the actin cytoskeleton in VE-cad^{DEE}-expressing cells. These cells exhibited an increase

in thick, parallel bundles around the cell periphery and decreased radial actin fibers, a pattern characteristic of stable junctions. These data suggest a role for cadherin endocytosis in permitting the reorganization of the actin cytoskeleton during the onset of polarized migration, but the precise mechanism of this regulation is currently unknown. Classic cadherins have been implicated in polarization and collective cell movements by directing migration machinery and protrusive activity away from cell-cell contacts and toward the leading edge (Desai et al., 2009; Dupin et al., 2009; Theveneau et al., 2010; Weber et al., 2012). Although the mechanisms that promote cadherin-mediated polarization are poorly understood, they may involve anisotropic distribution of cadherin molecules or asymmetric signaling from cadherin-mediated junctions, which could be disrupted in the stabilized VE-cad^{DEE/DEE} mutant (Dorland et al., 2016; Hayer et al., 2016; Mayor and Etienne-Manneville, 2016). Previous studies have implicated cadherin treadmilling along lateral borders, as well as endocytosis and recycling, in the process of collective cell migration (Peglion et al., 2014). Also, Cao et al. (2017) found that VEGF-induced polarized cell elongation during endothelial collective migration involves a reduction in the relative concentration of VE-cad at junctions. This reduction in cadherin triggers the formation of small, actin-driven junction-associated intermittent lamellipodia, which are associated with increased migration (Abu Taha et al., 2014; Cao et al., 2017). Combined with the results presented here showing that VE-cad endocytosis drives actin dynamics during collective migration, it is attractive to speculate that VE-cad endocytosis may promote junction-associated intermittent lamellipodia formation that, in turn, is required for polarization and collective migration. Additional studies will be required to fully understand how cadherin dynamics and actin organization are modulated by endocytic pathways to permit polarized endothelial cell migration in normal development and pathological circumstances such as tumor angiogenesis.

Materials and methods

Mice

Tie2-Cre mice (004128) and VE-cad-Cre mice (017968) were obtained from Jackson Laboratory and have been described previously (Chen et al., 2009; Koni et al., 2001). Mice with LoxP sites in introns 2 and 8 of the p120 gene were described previously (Davis and Reynolds, 2006). We generated point mutant mice with alanine substitutions in either DEE residues (aa 646–648) or GGG residues (aa 649–651) using CRISPR/Cas9 genome editing in conjunction with the Mouse Transgenic and Gene Targeting Core Facility at Emory. The CRISPR gRNA sequence 5'-CAGTTGGTCACTTACGATG-3' used for both mutants contains at least three base-pair mismatches against any other targets in the mouse genome. Long, single-stranded oligonucleotides containing the indicated point mutations at either the DEE or GGG site were injected into the cytoplasm of one-cell zygotes together with Cas9 mRNA and the gRNA. Founder pups with DEE or GGG point mutations generated by homology-directed repair with the donor oligonucleotide were identified by PCR/restriction fragment length polymorphism analysis of

genomic DNA. Primers CM13, 5'-CTGGTCCCATGAACCTGTCT-3' and CM14, 5'-GCGCACAGAATTAAGCACTG-3', were used to amplify a 212-bp product, which was digested with Fnu4H1. Both DEE and GGG mutant alleles contain a new Fnu4H1 site absent in the WT allele PCR product. The correct mutations were also confirmed by Sanger sequencing of genomic DNA. The Δ JMD mouse strain containing a deletion of amino acid residues 642–653 (LVTYDEEGGGE) was generated as a result of nonhomologous end joining during the process of making the DEE point mutant strain. The STOP allele of VE-cad contains a TGA stop codon at aa 647 and an aspartic-acid-to-leucine point mutation at aa 646 and was also generated by nonhomologous end joining while making the DEE point mutant strain. For body weight analysis of 3-wk-old mice, 19 female mutants, 26 male mutants, 38 female WT, and 20 male WT mice were weighed. For body weight analysis of 6-wk-old mice, 9 female mutants, 17 male mutants, 14 female WT, and 17 male WT mice were weighed. Data distribution was assumed to be normal, but this was not formally tested. Significance was evaluated using a two-tailed *t* test. All procedures were performed in accordance with National Institutes of Health guidelines and the US Public Health Service's Guide for the Care and Use of Laboratory Animals and were approved by the Institutional Animal Care and Use Committee of Emory University, which is accredited by the American Association for Accreditation of Laboratory Care.

Aorta en face immunostaining

6- to 8-week-old mice were euthanized by CO₂ inhalation and immediately perfused through the left ventricle with Dulbecco's PBS (DPBS) containing 10,000 U/L heparin followed by fresh 4% PFA in DPBS for 8 min. The thoracic aorta was then carefully removed and cleaned of fat in a Petri dish containing DPBS. The aorta was opened to expose the lumen and cut into pieces for immunostaining. Aortas were incubated two times in permeabilization buffer (0.25% Triton X-100 in DPBS) for 20 min at room temperature followed by incubation in blocking buffer (10% normal goat serum plus 0.25% Triton X-100 in DPBS) for 2 h at room temperature. Samples were then incubated overnight at 4°C with primary antibodies diluted in blocking buffer. Primary antibodies were rat anti-VE-cad (BV13, eBioscience 14144181, 1:500); rabbit anti-p120 (S-19, Santa Cruz Biotechnology sc-1101, 1:250); mouse anti- β -catenin (BD Biosciences 610153, 1:250); and mouse anti-N-cadherin (BD Biosciences 610920, 1:250). Aortas were washed four times in DPBS for 15 min each and incubated with secondary antibodies diluted in blocking buffer for 2 h at room temperature in the dark. Secondary antibodies were Alexa Fluor 555 goat anti-rat IgG (Invitrogen A-21434, 1:3,000); Alexa Fluor 488 goat anti-rabbit IgG (Invitrogen A-11008, 1:3,000); and Alexa Fluor 488 goat anti-mouse IgG (Invitrogen A-11029, 1:3,000). Samples were washed four times in DPBS and then mounted on glass slides with intima side up using ProLong Gold (Invitrogen P36930). Aortas were imaged with either a Zeiss LSM510 Meta confocal microscope with Zen 2009 software (40 \times /1.3-NA oil-immersion objective) or an Olympus FV1000 upright confocal microscope with Olympus Fluoview v4.2 acquisition software (40 \times /1.3-NA oil-immersion objective). At least four to six fields of view were

imaged from each mutant and WT littermate control. At least four separate litters were analyzed for each mutant, and all comparisons were made in similar regions of the aorta between mutant and WT. Images were analyzed using Nikon NIS-Elements AR version 4.40 software and processed using ImageJ (National Institutes of Health). The protein expression levels at cell–cell borders were quantitated by creating a mask of the borders in each field based on anti-VE-cad immunostaining and measuring the average fluorescent intensity of the protein of interest within this mask. Protein levels in WT were set to 100% for each litter, and the average percentage decrease in the indicated homozygous mutant littermate was quantitated. Statistics were computed using GraphPad Prism 7, and the Mann-Whitney *U* test was used to evaluate significance.

Eye cup and retina angiogenesis analysis

P3 mice were euthanized by decapitation. For lectin staining, eyes were enucleated and immediately fixed overnight at 4°C in 4% PFA in DPBS. Fixed eye cups were photographed for blood spots on a Nikon SMZ745T stereo Microscope with a Nikon DS-Fi3 Digital Camera + DS-L4 control unit. Blood spot area was quantitated using ImageJ, with a total of 16–20 mutants analyzed for each genotype, from at least four separate litters. A two-tailed *t* test was used to evaluate significance. Data distribution was assumed to be normal, but this was not formally tested. Eyes were then washed five times in DPBS, and retinas were dissected out and flattened by making four radial incisions. Retinas were then incubated in blocking buffer (0.3% Triton X-100 plus 10 mg/ml BSA in DPBS) overnight at 4°C. The next day, retinas were incubated overnight at 4°C with fluorescein-labeled *Griffonia simplicifolia* Lectin I isolectin B4 (GSL I-B4; Vector Laboratories FL-1201) diluted 1:50 in blocking buffer. Samples were then washed and mounted on glass slides using ProLong Gold (Invitrogen P36930). Images were acquired on a Zeiss LSM510 Meta confocal microscope (20 \times /0.75-NA dry objective) and stitched together using the stitching plugin from ImageJ. Vascular density, total vessel length, and branchpoints per unit area at the vascular front were quantitated using Angiotool software (National Institutes of Health, National Cancer Institute; Zudaire et al., 2011). Radial outgrowth was analyzed by measuring the radial distance from the optic nerve head to the vascular front at the retinal periphery. A Shapiro–Wilk test was used to confirm normal distribution of the data, and a paired *t* test between WT and mutant littermates was used to evaluate significance.

Embryo and yolk sac analysis

For timed pregnancies, the morning of the plug was designated as E0.5, and the day of birth, postnatal day 0 (P0). Whole unfixed embryos were harvested at E12.5 and examined and photographed on a Nikon SMZ745T stereo Microscope with a Nikon DS-Fi3 Digital Camera + DS-L4 control unit. For yolk sac analysis, WT and mutant littermates were harvested at E9.5 or E12.5, and yolk sacs were removed and fixed in 4% PFA in DPBS for 1.5 h at room temperature. This was followed by two DPBS washes. Samples were then incubated in blocking buffer (10% normal goat serum plus 0.1% Triton-X-100 in DPBS) for 2 h at

room temperature followed by overnight incubation at 4°C with anti-PECAM-1 (MEC13.3, BD Bioscience 550274, 1:250) diluted in blocking buffer. The next day, four washes in DPBS plus 0.1% Triton X-100 were performed, followed by incubation with Alexa Fluor 555 goat anti-rat IgG secondary antibody (Invitrogen A-21434, 1:3,000) for 2 h at room temperature in the dark. After four more washes, samples were mounted using ProLong Gold (Invitrogen P36930). Overlapping images of the entire E9.5 yolk sacs were taken on either a Zeiss LSM510 Meta confocal microscope (20×/0.75-NA dry objective) or an Olympus FV1000 upright confocal microscope (20×/0.75-NA dry objective). Images were stitched together using the stitching plugin from ImageJ. Vascular density, total vessel length, and branchpoints at comparable regions of the stitched yolk sacs were analyzed using Angiotool software. Quantitation was based on four to seven pairs of images within the yolk sac for each set of embryos (paired for corresponding locations within the yolk sac). A total of 25 image pairs from five separate litters were analyzed. A D'Agostino–Pearson normality test was performed to confirm a normal distribution of the data, and a paired *t* test between location-paired images from the WT and mutant was used to evaluate significance.

p120 conditional knockout rescue

To analyze rescue of VE-cad levels in p120CKO mice by the DEE mutant allele, matings were set up between VE-cad-Cre⁺; VE-cad^{DEE/+}; p120^{lox/lox} and VE-cad^{DEE/+}; p120^{lox/lox} mice to generate both VE-cad-Cre⁺; VE-cad^{+/+}; p120^{lox/lox} and VE-cad-Cre⁺; VE-cad^{DEE/DEE}; p120^{lox/lox} mice for analysis. VE-cad-Cre-mediated deletion of p120 resulted in mosaic deletion of p120, leading to fields of view with both p120⁺ and p120⁻ cells. To quantitate VE-cad levels, cell–cell borders between two p120⁺ or two p120⁻ cells were traced in ImageJ, and the average VE-cad levels were measured. The p120⁺ and p120⁻ borders were from the same field, and the average VE-cad level at the p120⁺ cell–cell borders in each sample was normalized to 100%. At least 5–10 fields of view (≥10 p120⁺ and 10 p120⁻ borders per field) from three independent experiments were analyzed for each genotype. Two-tailed *t* test was to evaluate significance. To analyze lethality rescue by the VE-cad DEE mutant allele, matings were set up between male Tie2-Cre; VE-cad^{DEE/+}; p120^{lox/lox} mice and female VE-cad^{DEE/+}; p120^{lox/lox} mice, and surviving offspring were genotyped between P6 and P8.

Aortic ring assay

Aortic ring assays were performed as described (Baker et al., 2011). Briefly, mice were sacrificed by CO₂ inhalation, and the thoracic aorta was dissected out under sterile conditions and transferred to a Petri dish containing cold Opti-MEM I reduced-serum medium + GlutaMAX-I (Gibco BRL 51985-026). Extraneous fat was removed, and blood was gently flushed from the vessel using a 27-G needle fixed to a 1-ml syringe. Using a scalpel, ~1-mm-wide aortic rings were cut and embedded in Matrigel (BD Biosciences 354230) in a 24-well plate. Aortic rings were incubated for 5–9 d at 37°C and 5% CO₂ in the above Opti-MEM medium supplemented with 100 U/ml penicillin and 100 µg/ml streptomycin (Gibco BRL 15140-122) and 2.5% (vol/vol) FBS.

Medium was removed every other day and replaced with 1 ml of fresh medium. Sprout outgrowth was imaged by phase microscopy using a BioTek Lionheart FX microscope equipped with a Point Grey GS3-U3-14S5M CCD camera and a 4× dry objective. The total area of vessel outgrowth minus the area of the ring was quantitated by a blinded observer using ImageJ, and results are representative of four independent experiments from separate litters, with ≥8–12 rings analyzed per experiment per animal. A D'Agostino–Pearson normality test was performed to confirm a normal distribution of the data, and a two-tailed *t* test was used to evaluate significance.

In vivo lung permeability assays

Lung permeability was measured using Evans blue dye leakage (Radu and Chernoff, 2013). Briefly, 2–3-mo-old mice received intraperitoneal injections of either normal DPBS or 18 mg/kg of body weight *E. coli* LPS (Sigma-Aldrich L4391, lot 043M4089V) in DPBS. After 6 h, mice were injected intraorbitally with 100 µl of 1% Evans blue solution (MP Biomedicals lot QR12404) in DPBS. Evans blue was allowed to circulate for 15 min, and mice were transcardially perfused with 50 ml of DPBS. The lungs were removed, and Evans blue was extracted by incubation with formamide at 55°C overnight. Dye concentration was quantitated spectrophotometrically in the supernatant at 620 nm and normalized to the dry weight of the lung. Statistics were computed using GraphPad Prism 7. Normal data distribution was confirmed using a Shapiro–Wilk test, and significance was evaluated using two-way ANOVA.

Cell culture

Primary mouse dermal endothelial cells were obtained using methods previously described (Oas et al., 2010). Briefly, skins from early postnatal pups (P5–P7) were isolated and enzymatically dissociated using 2 mg/ml collagenase type I (Worthington Biochemical Corp. LS004196) followed by trituration with a cannula. Endothelial cells were then purified by 10-min incubation in suspension with magnetic sheep anti-rat Dynabeads (Invitrogen) coated with rat anti-mouse PECAM-1 (rat; clone MEC13.3, BD Biosciences 553369). Magnetically sorted cells were then plated in flasks coated with 0.1% gelatin and grown to confluence. A second round of purification was then performed with anti-rat Dynabeads coated with rat anti-mouse ICAM-2 (rat clone 3C4; BD Biosciences 553325). Cells were cultured in Endothelial Cell Growth Medium MV2 (PromoCell C-22022). The endothelial identity of the cells was confirmed by immunofluorescence microscopy with antibodies to endothelial markers PECAM-1 and VE-cadherin. Greater than 95% purity was routinely observed in the preparations. Freshly isolated HUVECs were cultured in Endothelial Cell Growth Medium (PromoCell C-22010). Primary human dermal MECs were isolated from neonatal foreskin and cultured on 0.1% gelatin-coated culture dishes in 0.1% gelatin-coated culture dishes in EGM-2 MV media (Lonza cc-3202). Both HUVECs and MECs were used before passage 5 in all experiments, and the endothelial identity of the cells was confirmed by immunofluorescence microscopy with antibodies to endothelial markers PECAM-1 and VE-cadherin.

Western blotting

Isolated dermal endothelial cells were lysed in Laemmli sample buffer, and proteins were separated on a 7.5% Mini-Protean TGX precast gel (Bio-Rad 456-1025) using Tris/glycine/SDS running buffer (Bio-Rad 161-0732) and transferred to a nitrocellulose membrane (Thermo Fisher Scientific 88018). Western blots were developed with chemiluminescence HRP substrate (GE Healthcare RPN2106). Antibodies used were goat anti-VE-cad (C-19; Santa Cruz Biotechnology sc-6458; 1:500), rabbit anti-p120 (S-19; Santa Cruz Biotechnology sc-1101; 1:750), mouse anti- β -catenin (BD Biosciences 610153; 1:1,000), mouse anti-N-cadherin (BD Biosciences 610920; 1:1,000), and rabbit β -actin (clone D6A8; Cell Signaling Technology 8457S; 1:1,500). The chemiluminescent blots were imaged with a ChemiDoc MP imager (Bio-Rad). Densitometric analysis was performed using ImageJ.

Wounding assay

Primary mouse endothelial cells were plated in growth medium in 35-mm Culture-Insert 3-well wounding assay dishes (Ibidi 80366) and grown to confluence. Cells were then starved overnight in EBM-2 basal medium (Lonza cc-3156) containing 1% FBS. The next morning, the silicone insert was removed, leaving a 500- μ m wound. Each field was imaged by phase contrast with a 10 \times dry objective (0.3 NA) at initiation of wound closure and the indicated time points to monitor wound closure. Images were obtained using a Nikon Eclipse Ti-E Inverted Microscope equipped with a motorized stage and a Hamamatsu C11440-22CU Digital Camera and NIS-Elements software version AR4.40.00. Cells were maintained at 37°C in 5% CO₂ during imaging. Wound area was measured using ImageJ. A D'Agostino–Pearson normality test was performed to confirm normal distribution of the data, and a two-tailed *t* test was used to evaluate significance at each time point.

Golgi reorientation

Wounding assays with primary mouse cells were performed as described above. Cells were fixed at the indicated time point with 4% PFA in DPBS for 10 min at room temperature. Cells were washed with DPBS and permeabilized in 0.1% Triton X-100 in PBS for 10 min. Cells were incubated in blocking buffer (0.1% Triton X-100 plus 10% normal goat serum in DPBS) for 20 min followed by overnight incubation in primary antibodies at 4°C (mouse anti-GM-130, BD Transduction Laboratories 610822; 1:250; rat anti-VE-cad BV13, Thermo Fisher Scientific 14-1441-82; 1:500) diluted in blocking buffer. Cells were then incubated with an Alexa Fluor 488 goat anti-mouse IgG antibody (Invitrogen A-11029; 1:3,000) together with Alexa Fluor 555 goat anti-rat IgG (Invitrogen A-21434; 1:3,000) for 1 h at room temperature and mounted using ProLong Gold with DAPI (Invitrogen P36932). HUVECs were plated on gelatin-coated Ibidi wounding assay dishes (described above) or gelatin-coated coverslips in four-well dishes (Thermo Fisher Scientific, Nunc 144444) and infected with the indicated RFP-tagged lentivirus or adenovirus constructs. 3 d (for lentivirus) or 8 h (for adenovirus) after infection, cells were starved overnight in EBM-2 basal medium containing 1% FBS. The next morning, inserts were removed (or

cells were scratched with a pipette tip), and cells were allowed to polarize for 2–3 h as indicated. Cells were then fixed, immunostained for GM-130 and RFP (rabbit polyclonal anti-RFP; Rockland 600-401-379), and imaged. For CytoD experiments, HUVECs infected with VE-cadWT-RFP or VE-cadDEE-RFP adenovirus were treated for 2 h with 1 μ M CytoD (Sigma-Aldrich C8273) immediately after wounding, washed three times in DPBS, and allowed to polarize in complete medium for 3 h following washout. Untreated VE-cadWT-RFP and VE-cadDEE-RFP cells were allowed to polarize for 3 h following wounding. Human MECs plated on gelatin-coated coverslips in four-well dishes were infected in the morning with the indicated RFP-tagged adenovirus constructs and starved overnight. The next morning (24 h after infection), cells were wounded with a pipette tip and allowed to polarize for 6 h. Cells were then fixed, immunostained for GM-130 and RFP, and imaged. Mouse cell and HUVEC images were captured using a Nikon Eclipse Ti-E Inverted Microscope equipped with a motorized stage, a 60 \times /1.49-NA oil-immersion lens, and a Hamamatsu C11440-22CU Digital Camera using NIS-Elements software version AR4.40.00. MEC microscopy was performed using an epifluorescence microscope (DMRXA2, Leica) equipped with a 63 \times /1.32-NA oil-immersion objective, narrow bandpass filters, and a digital camera (ORCA-ER C4742-80, Hamamatsu Photonics). MEC images were captured using Simple PCI software (Hamamatsu Photonics). Wound edge cells with the Golgi apparatus localized within the 90° angle in front of the nucleus, facing the wound axis, were quantified as polarized. Angles were determined using ImageJ. Statistics were computed using GraphPad Prism 7. Data distribution was assumed to be normal, but this was not formally tested. For mouse cells, a total of 100 cells from each of four independent experiments were analyzed, and significance was evaluated using two-proportion Z test. For both HUVEC and MEC experiments, ≥ 60 cells from each of three independent experiments were analyzed, and significance was evaluated using one-way ANOVA with Tukey post hoc test.

F-actin analysis

To calculate average F-actin intensity, the VE-cad-RFP signal was used to outline individual cell borders at the wound edge, and the mean intensity of phalloidin-488 per each cell was measured using ImageJ. To measure the area of each cell that contains F-actin, we manually applied a threshold to the 16-bit image of phalloidin-488. The outlines of individual cells at the wound edge were traced, and the threshold area within each cell was measured. All samples were blinded before image acquisition and revealed after image analysis was completed. At least 50 cells from each of three independent experiments were analyzed. Data distribution was assumed to be normal, but this was not formally tested. Significance was evaluated using a two-tailed *t* test.

Live cell imaging

HUVECs were cultured, as described above, in 35-mm 4-well CELLview glass-bottom dishes (Greiner Bio-One 627870) coated with gelatin. Cells were infected with LifeAct-GFP lentivirus for 2 d and then transduced again with either VE-cadWT-RFP or VE-cadDEE-RFP adenovirus. 8 h after adenoviral infection, cells

were starved overnight in EBM-2 basal medium containing 1% FBS. Cells were manually scratched with a p200 pipette tip the next morning, and the starvation medium was replaced with phenol red-free growth medium. Dishes were placed on the microscope stage and maintained at 37°C in 5% CO₂ using a humidified temperature/CO₂-controlled chamber (Tokai Hit). Cells were imaged using a Nikon Eclipse Ti-E inverted microscope (60x/1.49-NA Apo TIRF oil-immersion objective) equipped with a motorized stage and a Hamamatsu C11440-22CU digital camera. Images were taken once per minute for 2 h, beginning 1 h after cells were scratched. Endocytic budding from the rear of wound-edge cells was quantitated by a blinded observer. At least eight videos were analyzed per condition, and significance was evaluated using a *t* test.

Virus production

For adenovirus virus production, VE-cad constructs were subcloned between BamHI and AgeI restriction sites in Gateway TagRFP-AS-N (Evrogen), in-frame with monomeric C-terminal RFP, then shuttled into pAd/Cmv/V5-DEST using LR Clonase recombination (Life Technologies). The vector was linearized using PacI and transfected into virus-producing QBI-293A cells. After 48–72 h, cells were lysed, and virus was harvested. The pLenti.PGK.LifeAct-GFP.W was a gift from Rusty Lansford (University of Southern California, Los Angeles, CA; Addgene plasmid 51010). To create replication-deficient second-generation lentivirus packaged with the indicated VE-cad gene containing a monomeric C-terminal RFP tag, the gene was cloned into pLenti6/V5-DEST and transfected into HEK-293T cells together with the necessary lentiviral regulatory genes. Lentivirus was collected from culture supernatants 48–72 h after transfection and concentrated by high-speed centrifugation.

Online supplemental material

Fig. S1 shows genotyping analysis of offspring from VE-cad^{GGG/GGG} × VE-cad^{STOP/+} matings, quantitation of blood spot area in the retinas of VE-cad^{GGG/GGG} mutants, analysis of VE-cad and p120 protein expression levels in dermal endothelial cell lysates from VE-cad mutant mice, and immunostaining analysis of β-catenin expression in VE-cad^{GGG/GGG} mutant aortas. **Fig. S2** shows the quantitation of blood spot area in the retinas of VE-cad^{ΔJMD/ΔJMD} and VE-cad^{DEE/DEE} mutant mice and the immunostaining analysis of VE-cad and β-catenin levels at cell–cell junctions in the aortas of VE-cad^{DEE/DEE} mice. **Fig. S3** shows the scratch-wound analysis of VE-cad^{GGG/GGG} mutant dermal endothelial cells and the Golgi reorientation defects observed in human MECs expressing VE-cadDEE mutant. **Fig. S4** shows representative time-lapse images of wound-edge HUVECs transduced with LifeAct-GFP (green) and either VE-cadWT-RFP or VE-cadDEE-RFP. **Fig. S5** shows the individual channels from cells shown in **Fig. 8 D** before and after CytoD treatment.

Acknowledgments

We thank Drs. B. Petrich and P. Vincent for reviewing the manuscript, members of the Kowalczyk laboratory for their help and advice, and M. Myers for fruitful discussions.

This work was supported by grants from the National Institutes of Health (R01AR050501 and R01AR048266 to A.P. Kowalczyk and HL095070 to K.K. Griendling). This research project was supported in part by the Emory University Integrated Cellular Imaging Microscopy Core of the Winship Cancer Institute comprehensive cancer center grant, P30CA138292. This study was supported in part by the Mouse Transgenic and Gene Targeting Core and the Emory Integrated Genomics Core, which are subsidized by the School of Medicine, Emory University, and are Emory Integrated Core Facilities. Additional support was provided by the Georgia Clinical & Translational Science Alliance of the National Institutes of Health under Award Number UL1TR002378. The content is solely the responsibility of the authors and does not necessarily reflect the official views of the National Institutes of Health.

The authors declare no competing financial interests.

Author contributions: C.M. Grimsley-Myers, C.M. Cadwell, R.H. Isaacson, J. Campos, K.R. Myers, T. Seo, and M.S. Hernandez performed the experiments and analyzed results. W. Giang performed data analysis. C.M. Grimsley-Myers, C.M. Cadwell, M.S. Hernandez, K.R. Myers, K.K. Griendling, and A.P. Kowalczyk designed the experiments. C.M. Grimsley-Myers and A.P. Kowalczyk wrote the manuscript. All authors reviewed and approved the final version of the manuscript.

Submitted: 13 September 2019

Revised: 10 January 2020

Accepted: 28 February 2020

References

- Abraham, S., M. Yeo, M. Montero-Balaguer, H. Paterson, E. Dejana, C.J. Marshall, and G. Mavria. 2009. VE-Cadherin-mediated cell-cell interaction suppresses sprouting via signaling to MLC2 phosphorylation. *Curr. Biol.* 19:668–674. <https://doi.org/10.1016/j.cub.2009.02.057>
- Abu Taha, A., M. Taha, J. Seebach, and H.J. Schnittler. 2014. ARP2/3-mediated junction-associated lamellipodia control VE-cadherin-based cell junction dynamics and maintain monolayer integrity. *Mol. Biol. Cell.* 25:245–256. <https://doi.org/10.1091/mbc.e13-07-0404>
- Anastasiadis, P.Z. 2007. p120-ctn: A nexus for contextual signaling via Rho GTPases. *Biochim. Biophys. Acta.* 1773:34–46. <https://doi.org/10.1016/j.bbamcr.2006.08.040>
- Anastasiadis, P.Z., and A.B. Reynolds. 2001. Regulation of Rho GTPases by p120-catenin. *Curr. Opin. Cell Biol.* 13:604–610. [https://doi.org/10.1016/S0955-0674\(00\)0258-1](https://doi.org/10.1016/S0955-0674(00)0258-1)
- Anastasiadis, P.Z., S.Y. Moon, M.A. Thoreson, D.J. Mariner, H.C. Crawford, Y. Zheng, and A.B. Reynolds. 2000. Inhibition of RhoA by p120 catenin. *Nat. Cell Biol.* 2:637–644. <https://doi.org/10.1038/35023588>
- Arima, S., K. Nishiyama, T. Ko, Y. Arima, Y. Hakoizaki, K. Sugihara, H. Koseki, Y. Uchijima, Y. Kurihara, and H. Kurihara. 2011. Angiogenic morphogenesis driven by dynamic and heterogeneous collective endothelial cell movement. *Development.* 138:4763–4776. <https://doi.org/10.1242/dev.068023>
- Baker, M., S.D. Robinson, T. Lechertier, P.R. Barber, B. Tavora, G. D'Amico, D.T. Jones, B. Vojnovic, and K. Hodivala-Dilke. 2011. Use of the mouse aortic ring assay to study angiogenesis. *Nat. Protoc.* 7:89–104. <https://doi.org/10.1038/nprot.2011.435>
- Bentley, K., C.A. Franco, A. Philippides, R. Blanco, M. Dierkes, V. Gebala, F. Stanchi, M. Jones, I.M. Aspalter, G. Cagna, et al. 2014. The role of differential VE-cadherin dynamics in cell rearrangement during angiogenesis. *Nat. Cell Biol.* 16:309–321. <https://doi.org/10.1038/ncb2926>
- Betz, C., A. Lenard, H.G. Belting, and M. Affolter. 2016. Cell behaviors and dynamics during angiogenesis. *Development.* 143:2249–2260. <https://doi.org/10.1242/dev.135616>
- Bulgakova, N.A., and N.H. Brown. 2016. Drosophila p120-catenin is crucial for endocytosis of the dynamic E-cadherin-Bazooka complex. *J. Cell Sci.* 129:477–482. <https://doi.org/10.1242/jcs.177527>

- Cadwell, C.M., W. Su, and A.P. Kowalczyk. 2016. Cadherin tales: Regulation of cadherin function by endocytic membrane trafficking. *Traffic*. 17: 1262–1271. <https://doi.org/10.1111/tra.12448>
- Cao, J., M. Ehling, S. März, J. Seebach, K. Tarbashevich, T. Sixta, M.E. Pitulescu, A.C. Werner, B. Flach, E. Montanez, et al. 2017. Polarized actin and VE-cadherin dynamics regulate junctional remodelling and cell migration during sprouting angiogenesis. *Nat. Commun.* 8:2210. <https://doi.org/10.1038/s41467-017-02373-8>
- Carmeliet, P., and R.K. Jain. 2011. Principles and mechanisms of vessel normalization for cancer and other angiogenic diseases. *Nat. Rev. Drug Discov.* 10:417–427. <https://doi.org/10.1038/nrd3455>
- Carmeliet, P., M.G. Lampugnani, L. Moons, F. Breviaro, V. Compernelle, F. Bono, G. Balconi, R. Spagnuolo, B. Oosthuysen, M. Dewerchin, et al. 1999. Targeted deficiency or cytosolic truncation of the VE-cadherin gene in mice impairs VEGF-mediated endothelial survival and angiogenesis. *Cell*. 98:147–157. [https://doi.org/10.1016/S0092-8674\(00\)81010-7](https://doi.org/10.1016/S0092-8674(00)81010-7)
- Chappell, J.C., D.M. Wiley, and V.L. Bautch. 2011. Regulation of blood vessel sprouting. *Semin. Cell Dev. Biol.* 22:1005–1011. <https://doi.org/10.1016/j.semcdb.2011.10.006>
- Chen, M.J., T. Yokomizo, B.M. Zeigler, E. Dzierzak, and N.A. Speck. 2009. Runx1 is required for the endothelial to haematopoietic cell transition but not thereafter. *Nature*. 457:887–891. <https://doi.org/10.1038/nature07619>
- Crosby, C.V., P.A. Fleming, W.S. Argraves, M. Corada, L. Zanetta, E. Dejana, and C.J. Drake. 2005. VE-cadherin is not required for the formation of nascent blood vessels but acts to prevent their disassembly. *Blood*. 105: 2771–2776. <https://doi.org/10.1182/blood-2004-06-2244>
- Davis, M.A., and A.B. Reynolds. 2006. Blocked acinar development, E-cadherin reduction, and intraepithelial neoplasia upon ablation of p120-catenin in the mouse salivary gland. *Dev. Cell*. 10:21–31. <https://doi.org/10.1016/j.devcel.2005.12.004>
- Davis, M.A., R.C. Ireton, and A.B. Reynolds. 2003. A core function for p120-catenin in cadherin turnover. *J. Cell Biol.* 163:525–534. <https://doi.org/10.1083/jcb.200307111>
- de Rooij, J., A. Kerstens, G. Danuser, M.A. Schwartz, and C.M. Waterman-Storer. 2005. Integrin-dependent actomyosin contraction regulates epithelial cell scattering. *J. Cell Biol.* 171:153–164. <https://doi.org/10.1083/jcb.200506152>
- Dejana, E., and D. Vestweber. 2013. The role of VE-cadherin in vascular morphogenesis and permeability control. *Prog. Mol. Biol. Transl. Sci.* 116: 119–144. <https://doi.org/10.1016/B978-0-12-394311-8.00006-6>
- Desai, R.A., L. Gao, S. Raghavan, W.F. Liu, and C.S. Chen. 2009. Cell polarity triggered by cell-cell adhesion via E-cadherin. *J. Cell Sci.* 122:905–911. <https://doi.org/10.1242/jcs.028183>
- Dorland, Y.L., T.S. Malinova, A.M. van Stalborch, A.G. Grieve, D. van Geemen, N.S. Jansen, B.J. de Kreuk, K. Nawaz, J. Kole, D. Geerts, et al. 2016. The F-BAR protein pacsin2 inhibits asymmetric VE-cadherin internalization from tensile adherens junctions. *Nat. Commun.* 7:12210. <https://doi.org/10.1038/ncomms12210>
- Duñach, M., B. Del Valle-Pérez, and A. García de Herreros. 2017. p120-catenin in canonical Wnt signaling. *Crit. Rev. Biochem. Mol. Biol.* 52:327–339. <https://doi.org/10.1080/10409238.2017.1295920>
- Dupin, I., E. Camand, and S. Etienne-Manneville. 2009. Classical cadherins control nucleus and centrosome position and cell polarity. *J. Cell Biol.* 185:779–786. <https://doi.org/10.1083/jcb.200812034>
- Elia, L.P., M. Yamamoto, K. Zang, and L.F. Reichardt. 2006. p120 catenin regulates dendritic spine and synapse development through Rho-family GTPases and cadherins. *Neuron*. 51:43–56. <https://doi.org/10.1016/j.neuron.2006.05.018>
- Fallah, A., A. Sadeghinia, H. Kahroba, A. Samadi, H.R. Heidari, B. Bradaran, S. Zeinali, and O. Molavi. 2019. Therapeutic targeting of angiogenesis molecular pathways in angiogenesis-dependent diseases. *Biomed. Pharmacother.* 110:775–785. <https://doi.org/10.1016/j.biopha.2018.12.022>
- Ferreri, D.M., F.L. Minnear, T. Yin, A.P. Kowalczyk, and P.A. Vincent. 2008. N-cadherin levels in endothelial cells are regulated by monolayer maturity and p120 availability. *Cell Commun. Adhes.* 15:333–349. <https://doi.org/10.1080/15419060802440377>
- Folkman, J. 2007. Angiogenesis: an organizing principle for drug discovery? *Nat. Rev. Drug Discov.* 6:273–286. <https://doi.org/10.1038/nrd2115>
- Friedl, P., and D. Gilmour. 2009. Collective cell migration in morphogenesis, regeneration and cancer. *Nat. Rev. Mol. Cell Biol.* 10:445–457. <https://doi.org/10.1038/nrm2720>
- Fruttiger, M. 2007. Development of the retinal vasculature. *Angiogenesis*. 10: 77–88. <https://doi.org/10.1007/s10456-007-9065-1>
- Frye, M., M. Dierkes, V. Küppers, M. Vockel, J. Tomm, D. Zeuschner, J. Rossaint, A. Zarbock, G.Y. Koh, K. Peters, et al. 2015. Interfering with VE-PTP stabilizes endothelial junctions in vivo via Tie-2 in the absence of VE-cadherin. *J. Exp. Med.* 212:2267–2287. <https://doi.org/10.1084/jem.20150718>
- Gaengel, K., C. Niaudet, K. Hagikura, B. Laviña, L. Muhl, J.J. Hofmann, L. Ebarasi, S. Nyström, S. Rymo, L.L. Chen, et al. 2012. The sphingosine-1-phosphate receptor S1PR1 restricts sprouting angiogenesis by regulating the interplay between VE-cadherin and VEGFR2. *Dev. Cell*. 23: 587–599. <https://doi.org/10.1016/j.devcel.2012.08.005>
- Garcia, M.D., and I.V. Larina. 2014. Vascular development and hemodynamic force in the mouse yolk sac. *Front. Physiol.* 5:308.
- Garrett, J.P., A.M. Lowery, A.P. Adam, A.P. Kowalczyk, and P.A. Vincent. 2017. Regulation of endothelial barrier function by p120-catenin•VE-cadherin interaction. *Mol. Biol. Cell*. 28:85–97. <https://doi.org/10.1091/mbc.e16-08-0616>
- Gentil-dit-Maurin, A., S. Oun, S. Almagro, S. Bouillot, M. Courçon, R. Linnepe, D. Vestweber, P. Huber, and E. Tillet. 2010. Unraveling the distinct distributions of VE- and N-cadherin in endothelial cells: a key role for p120-catenin. *Exp. Cell Res.* 316:2587–2599. <https://doi.org/10.1016/j.yexcr.2010.06.015>
- Geudens, I., and H. Gerhardt. 2011. Coordinating cell behaviour during blood vessel formation. *Development*. 138:4569–4583. <https://doi.org/10.1242/dev.062323>
- Giampietro, C., A. Taddei, M. Corada, G.M. Sarra-Ferraris, M. Alcalay, U. Cavallaro, F. Orsenigo, M.G. Lampugnani, and E. Dejana. 2012. Overlapping and divergent signaling pathways of N-cadherin and VE-cadherin in endothelial cells. *Blood*. 119:2159–2170. <https://doi.org/10.1182/blood-2011-09-381012>
- Giannotta, M., M. Trani, and E. Dejana. 2013. VE-cadherin and endothelial adherens junctions: active guardians of vascular integrity. *Dev. Cell*. 26: 441–454. <https://doi.org/10.1016/j.devcel.2013.08.020>
- Gory-Fauré, S., M.H. Prandini, H. Pointu, V. Roullot, I. Pignot-Paintrand, M. Vernet, and P. Huber. 1999. Role of vascular endothelial-cadherin in vascular morphogenesis. *Development*. 126:2093–2102.
- Hayer, A., L. Shao, M. Chung, L.M. Joubert, H.W. Yang, F.C. Tsai, A. Bisaria, E. Betzig, and T. Meyer. 2016. Engulfed cadherin fingers are polarized junctional structures between collectively migrating endothelial cells. *Nat. Cell Biol.* 18:1311–1323. <https://doi.org/10.1038/ncb3438>
- Helker, C.S., A. Schuermann, T. Karpanen, D. Zeuschner, H.G. Belting, M. Affolter, S. Schulte-Merker, and W. Herzog. 2013. The zebrafish common cardinal veins develop by a novel mechanism: lumen ensheathment. *Development*. 140:2776–2786. <https://doi.org/10.1242/dev.091876>
- Hendley, A.M., E. Provost, J.M. Bailey, Y.J. Wang, M.H. Cleveland, D. Blake, R.W. Bittman, J.C. Roeser, A. Maitra, A.B. Reynolds, and S.D. Leach. 2015. p120 Catenin is required for normal tubulogenesis but not epithelial integrity in developing mouse pancreas. *Dev. Biol.* 399:41–53. <https://doi.org/10.1016/j.ydbio.2014.12.010>
- Huveneers, S., and J. de Rooij. 2013. Mechanosensitive systems at the cadherin-F-actin interface. *J. Cell Sci.* 126:403–413. <https://doi.org/10.1242/jcs.109447>
- Huveneers, S., J. Oldenburg, E. Spanjaard, G. van der Krogt, I. Grigoriev, A. Akhmanova, H. Rehmann, and J. de Rooij. 2012. Vinculin associates with endothelial VE-cadherin junctions to control force-dependent remodeling. *J. Cell Biol.* 196:641–652. <https://doi.org/10.1083/jcb.201108120>
- Ishiyama, N., S.H. Lee, S. Liu, G.Y. Li, M.J. Smith, L.F. Reichardt, and M. Ikura. 2010. Dynamic and static interactions between p120 catenin and E-cadherin regulate the stability of cell-cell adhesion. *Cell*. 141:117–128. <https://doi.org/10.1016/j.cell.2010.01.017>
- Iyer, K.V., R. Piscitello-Gomez, J. Pajmans, F. Julicher, and S. Eaton. 2019. Epithelial Viscoelasticity Is Regulated by Mechanosensitive E-cadherin Turnover. *Curr. Biol.* 29:578–591.e575.
- Jakobsson, L., C.A. Franco, K. Bentley, R.T. Collins, B. Ponsioen, I.M. Aspalter, I. Rosewell, M. Busse, G. Thurston, A. Medvinsky, et al. 2010. Endothelial cells dynamically compete for the tip cell position during angiogenic sprouting. *Nat. Cell Biol.* 12:943–953. <https://doi.org/10.1038/ncb2103>
- Khalil, A.A., and J. de Rooij. 2019. Cadherin mechanotransduction in leader-follower cell specification during collective migration. *Exp. Cell Res.* 376: 86–91. <https://doi.org/10.1016/j.yexcr.2019.01.006>
- Koni, P.A., S.K. Joshi, U.A. Temann, D. Olson, L. Burkly, and R.A. Flavell. 2001. Conditional vascular cell adhesion molecule 1 deletion in mice: impaired lymphocyte migration to bone marrow. *J. Exp. Med.* 193:741–754. <https://doi.org/10.1084/jem.193.6.741>
- Kourtidis, A., S.P. Ngok, and P.Z. Anastasiadis. 2013. p120 catenin: an essential regulator of cadherin stability, adhesion-induced signaling, and

- cancer progression. *Prog. Mol. Biol. Transl. Sci.* 116:409–432. <https://doi.org/10.1016/B978-0-12-394311-8.00018-2>
- Kurley, S.J., B. Bierie, R.H. Carnahan, N.A. Lobdell, M.A. Davis, I. Hofmann, H.L. Moses, W.J. Muller, and A.B. Reynolds. 2012. p120-catenin is essential for terminal end bud function and mammary morphogenesis. *Development*. 139:1754–1764. <https://doi.org/10.1242/dev.072769>
- Legendijk, A.K., and B.M. Hogan. 2015. VE-cadherin in vascular development: a coordinator of cell signaling and tissue morphogenesis. *Curr. Top. Dev. Biol.* 112:325–352. <https://doi.org/10.1016/bs.ctdb.2014.11.024>
- le Duc, Q., Q. Shi, I. Blonk, A. Sonnenberg, N. Wang, D. Leckband, and J. de Rooij. 2010. Vinculin potentiates E-cadherin mechanosensing and is recruited to actin-anchored sites within adherens junctions in a myosin II-dependent manner. *J. Cell Biol.* 189:1107–1115. <https://doi.org/10.1083/jcb.201001149>
- Lenard, A., E. Ellertsdottir, L. Herwig, A. Krudewig, L. Sauteur, H.G. Belting, and M. Affolter. 2013. In vivo analysis reveals a highly stereotypic morphogenetic pathway of vascular anastomosis. *Dev. Cell*. 25:492–506. <https://doi.org/10.1016/j.devcel.2013.05.010>
- Luo, Y., and G.L. Radice. 2005. N-cadherin acts upstream of VE-cadherin in controlling vascular morphogenesis. *J. Cell Biol.* 169:29–34. <https://doi.org/10.1083/jcb.200411127>
- Mangold, S., S.K. Wu, S.J. Norwood, B.M. Collins, N.A. Hamilton, P. Thorn, and A.S. Yap. 2011. Hepatocyte growth factor acutely perturbs actin filament anchorage at the epithelial zonula adherens. *Curr. Biol.* 21:503–507. <https://doi.org/10.1016/j.cub.2011.02.018>
- Marciano, D.K., P.R. Brakeman, C.Z. Lee, N. Spivak, D.J. Eastburn, D.M. Bryant, G.M. Beaudoin III, I. Hofmann, K.E. Mostov, and L.F. Reichardt. 2011. p120 catenin is required for normal renal tubulogenesis and glomerulogenesis. *Development*. 138:2099–2109. <https://doi.org/10.1242/dev.056564>
- Mayor, R., and S. Etienne-Manneville. 2016. The front and rear of collective cell migration. *Nat. Rev. Mol. Cell Biol.* 17:97–109. <https://doi.org/10.1038/nrm.2015.14>
- Montero-Balaguer, M., K. Swirsding, F. Orsenigo, F. Cotelli, M. Mione, and E. Dejana. 2009. Stable vascular connections and remodeling require full expression of VE-cadherin in zebrafish embryos. *PLoS One*. 4:e5772. <https://doi.org/10.1371/journal.pone.0005772>
- Myster, S.H., R. Cavallo, C.T. Anderson, D.T. Fox, and M. Peifer. 2003. Drosophila p120catenin plays a supporting role in cell adhesion but is not an essential adherens junction component. *J. Cell Biol.* 160:433–449. <https://doi.org/10.1083/jcb.200211083>
- Nanes, B.A., C. Chiasson-MacKenzie, A.M. Lowery, N. Ishiyama, V. Faundez, M. Ikura, P.A. Vincent, and A.P. Kowalczyk. 2012. p120-catenin binding masks an endocytic signal conserved in classical cadherins. *J. Cell Biol.* 199:365–380. <https://doi.org/10.1083/jcb.201205029>
- Neto, F., A. Klaus-Bergmann, Y.T. Ong, S. Alt, A.C. Vion, A. Szymborska, J.R. Carvalho, I. Hollfinger, E. Bartels-Klein, C.A. Franco, et al. 2018. YAP and TAZ regulate adherens junction dynamics and endothelial cell distribution during vascular development. *eLife*. 7:e31037. <https://doi.org/10.7554/eLife.31037>
- Oas, R.G., B.A. Nanes, C.C. Esimai, P.A. Vincent, A.J. García, and A.P. Kowalczyk. 2013. p120-catenin and β -catenin differentially regulate cadherin adhesive function. *Mol. Biol. Cell*. 24:704–714. <https://doi.org/10.1091/mbc.e12-06-0471>
- Oas, R.G., K. Xiao, S. Summers, K.B. Wittich, C.M. Chiasson, W.D. Martin, H.E. Grossniklaus, P.A. Vincent, A.B. Reynolds, and A.P. Kowalczyk. 2010. p120-Catenin is required for mouse vascular development. *Circ. Res.* 106:941–951. <https://doi.org/10.1161/CIRCRESAHA.109.207753>
- Pacquelet, A., L. Lin, and P. Rorth. 2003. Binding site for p120/delta-catenin is not required for Drosophila E-cadherin function in vivo. *J. Cell Biol.* 160:313–319. <https://doi.org/10.1083/jcb.200207160>
- Peglion, F., F. Lense, and S. Etienne-Manneville. 2014. Adherens junction treadmill during collective migration. *Nat. Cell Biol.* 16:639–651. <https://doi.org/10.1038/ncb2985>
- Perez-Moreno, M., M.A. Davis, E. Wong, H.A. Pasolli, A.B. Reynolds, and E. Fuchs. 2006. p120-catenin mediates inflammatory responses in the skin. *Cell*. 124:631–644. <https://doi.org/10.1016/j.cell.2005.11.043>
- Potente, M., H. Gerhardt, and P. Carmeliet. 2011. Basic and therapeutic aspects of angiogenesis. *Cell*. 146:873–887. <https://doi.org/10.1016/j.cell.2011.08.039>
- Radu, M., and J. Chernoff. 2013. An in vivo assay to test blood vessel permeability. *J. Vis. Exp.* 16:e50062.
- Ratheesh, A., and A.S. Yap. 2010. Doing cell biology in embryos: regulated membrane traffic and its implications for cadherin biology. *FI000 Biol. Rep.* 27:30. <https://doi.org/10.3410/B2-30>
- Sauteur, L., A. Krudewig, L. Herwig, N. Ehrenfeuchter, A. Lenard, M. Affolter, and H.G. Belting. 2014. Cdh5/VE-cadherin promotes endothelial cell interface elongation via cortical actin polymerization during angiogenic sprouting. *Cell Rep.* 9:504–513. <https://doi.org/10.1016/j.celrep.2014.09.024>
- Schuermann, A., C.S. Helker, and W. Herzog. 2014. Angiogenesis in zebrafish. *Semin. Cell Dev. Biol.* 31:106–114. <https://doi.org/10.1016/j.semcdb.2014.04.037>
- Shapiro, L., and W.I. Weiss. 2009. Structure and biochemistry of cadherins and catenins. *Cold Spring Harb. Perspect. Biol.* 1:a003053. <https://doi.org/10.1101/cshperspect.a003053>
- Szymborska, A., and H. Gerhardt. 2018. Hold Me, but Not Too Tight—Endothelial Cell-Cell Junctions in Angiogenesis. *Cold Spring Harb. Perspect. Biol.* 10:a029223. <https://doi.org/10.1101/cshperspect.a029223>
- Theveneau, E., L. Marchant, S. Kuriyama, M. Gull, B. Moepps, M. Parsons, and R. Mayor. 2010. Collective chemotaxis requires contact-dependent cell polarity. *Dev. Cell*. 19:39–53. <https://doi.org/10.1016/j.devcel.2010.06.012>
- Tillet, E., D. Vittet, O. Féraud, R. Moore, R. Kemler, and P. Huber. 2005. N-cadherin deficiency impairs pericyte recruitment, and not endothelial differentiation or sprouting, in embryonic stem cell-derived angiogenesis. *Exp. Cell Res.* 310:392–400. <https://doi.org/10.1016/j.yexcr.2005.08.021>
- Udan, R.S., T.J. Vadakkan, and M.E. Dickinson. 2013. Dynamic responses of endothelial cells to changes in blood flow during vascular remodeling of the mouse yolk sac. *Development*. 140:4041–4050. <https://doi.org/10.1242/dev.096255>
- Vitorino, P., and T. Meyer. 2008. Modular control of endothelial sheet migration. *Genes Dev.* 22:3268–3281. <https://doi.org/10.1101/gad.1725808>
- Weber, G.F., M.A. Bjerke, and D.W. DeSimone. 2012. A mechanoresponsive cadherin-keratin complex directs polarized protrusive behavior and collective cell migration. *Dev. Cell*. 22:104–115. <https://doi.org/10.1016/j.devcel.2011.10.013>
- Zhang, J., M. Betson, J. Erasmus, K. Zeikos, M. Bailly, L.P. Cramer, and V.M. Braga. 2005. Actin at cell-cell junctions is composed of two dynamic and functional populations. *J. Cell Sci.* 118:5549–5562. <https://doi.org/10.1242/jcs.02639>
- Zudaire, E., L. Gambardella, C. Kurcz, and S. Vermeren. 2011. A computational tool for quantitative analysis of vascular networks. *PLoS One*. 6:e27385. <https://doi.org/10.1371/journal.pone.0027385>

Supplemental material

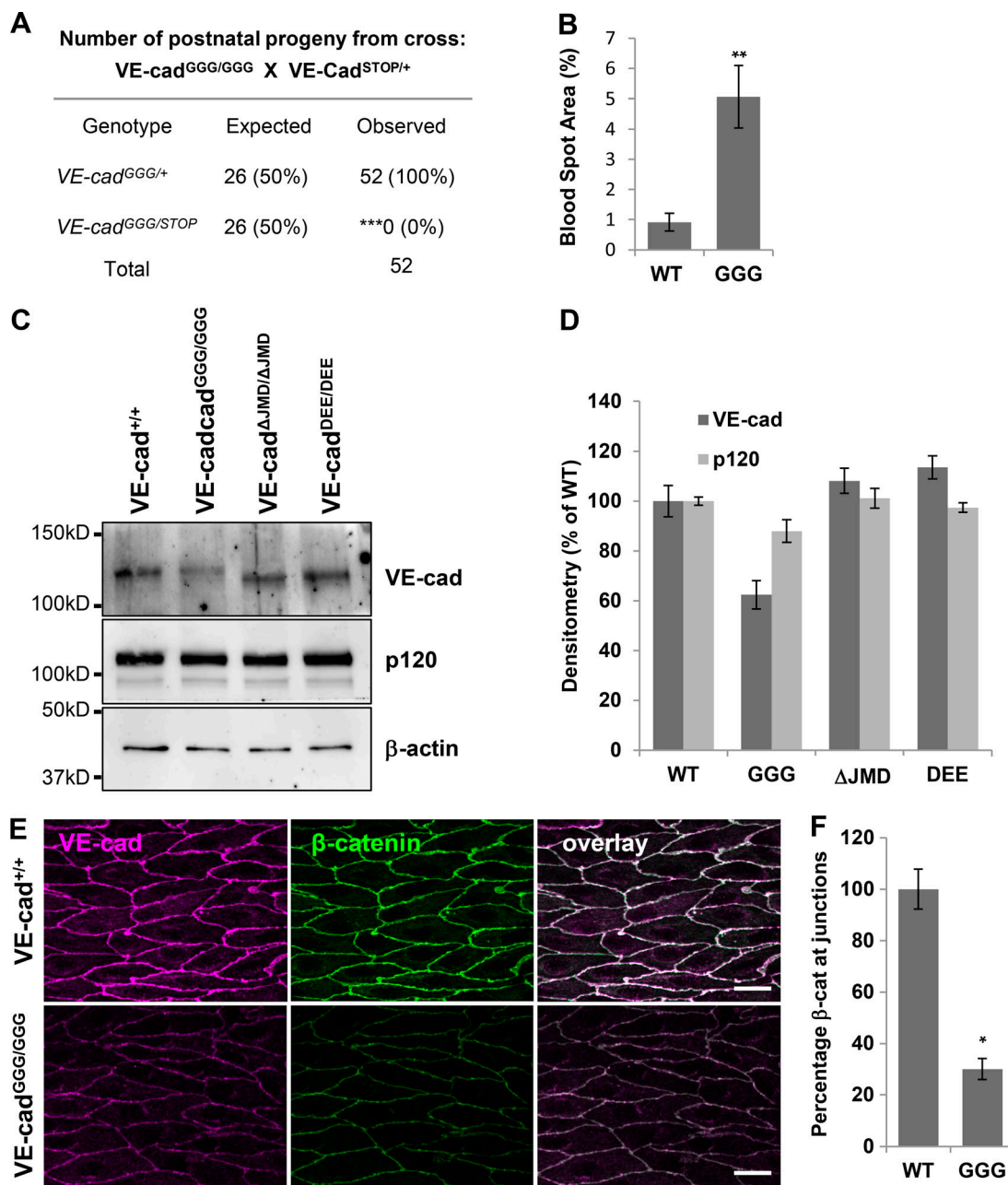


Figure S1. **Lethality, barrier, and junction defects in VE-cad^{GGG/GGG} mutants.** (A) Enhancement of the lethality phenotype in GGG mutants with one copy of VE-cad null VE-cad^{STOP} allele. Genotyping analysis of offspring from VE-cad^{GGG/GGG} × VE-cad^{STOP/+} matings revealed no surviving VE-cad^{GGG/STOP} pups. The expected number of mice was based on the total number of mice and expected Mendelian ratios. ***, $P < 0.001$ in χ^2 analysis. (B) Quantitation of blood spot area in VE-cad^{GGG/GGG} mutant and WT littermate retinas at P3. Area was quantitated from $n = 7$ (WT) and $n = 17$ (VE-cad^{GGG/GGG}). **, $P < 0.005$, t test. (C) Isolated dermal endothelial cell lysates were prepared from the indicated WT and mutant mice and run in duplicate on SDS-PAGE gels. Protein expression levels were analyzed by Western blotting using the indicated antibodies. (D) Densitometry of Western blot data, normalized to β -actin. Data were averaged from $n = 2$ independent experiments and are presented as mean \pm SEM. (E) Decreased β -catenin at cell-cell borders in VE-cad^{GGG/GGG} mutant mice. Aorta en face preparations were immunostained for VE-cad (magenta) and β -catenin (green). Scale bar: 20 μ m. (F) Quantitation of β -catenin levels at cell-cell junctions in the aortas of VE-cad^{+/+} and VE-cad^{GGG/GGG} mutant mice. β -Catenin levels were decreased in the mutant similarly to VE-cad. Levels were quantitated from four independent experiments with four to six images per animal. Results represent the relative mean \pm SEM. *, $P < 0.05$.

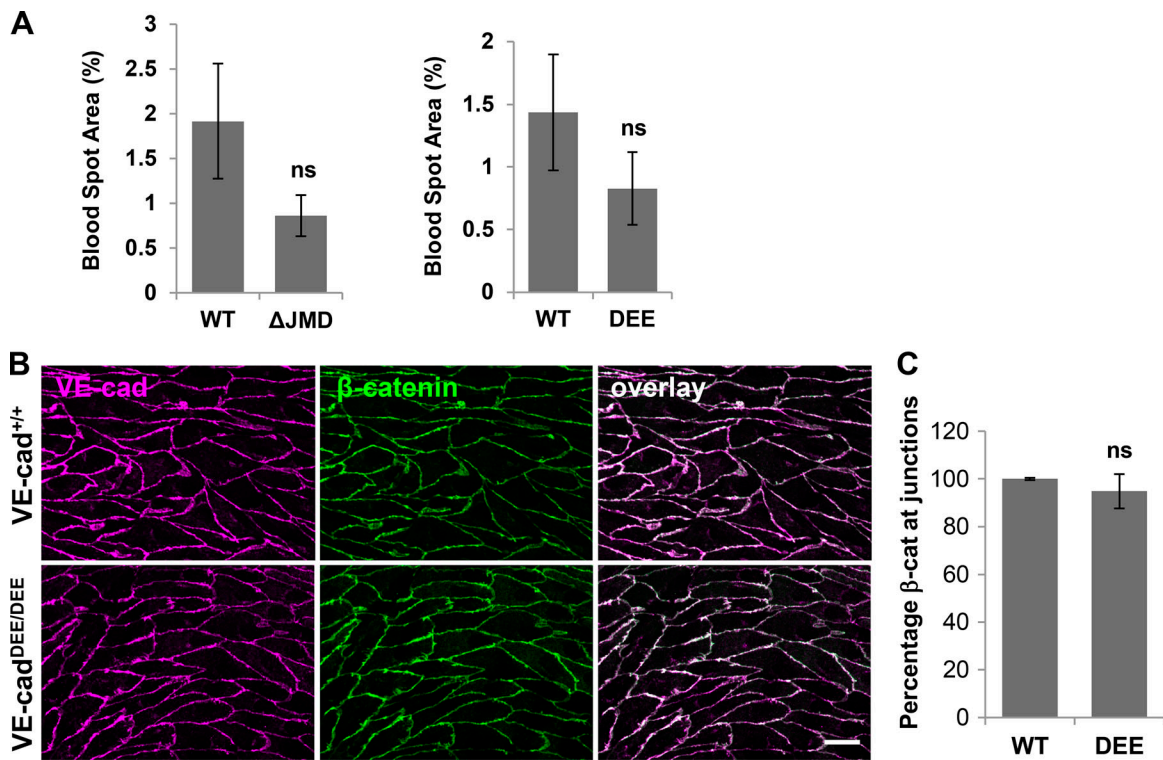


Figure S2. **Blood spot area in VE-cad ^{Δ JMD/ Δ JMD} and VE-cad^{DEE/DEE} mutant retinas and β -catenin immunostaining in VE-cad^{DEE/DEE} mutant aortas.** (A) Quantitation of blood spot area in the retinas of WT and VE-cad ^{Δ JMD/ Δ JMD} mutant littermates (left) and WT and VE-cad^{DEE/DEE} mutant littermates (right) at P3. Area was quantitated from $n = 14$ (WT littermates of VE-cad ^{Δ JMD/ Δ JMD}) and $n = 21$ (VE-cad ^{Δ JMD/ Δ JMD}) and $n = 12$ (WT littermates of VE-cad^{DEE/DEE}) and $n = 16$ (VE-cad^{DEE/DEE}); ns, not significant, t test. (B) Immunostaining analysis for VE-cad (magenta) and β -catenin (green) on en face aorta preparations from control and VE-cad^{DEE/DEE} mutant mice. β -Catenin levels and localization appeared normal in VE-cad^{DEE/DEE} mutant mice. Scale bar: 20 μ m. (C) Quantitation of VE-cad and β -catenin levels at cell-cell junctions in the aortas of VE-cad^{+/+} and VE-cad^{DEE/DEE} mice. Levels were quantitated from three independent experiments with four to six images per animal and are shown as the relative mean \pm SEM; ns, not significant.

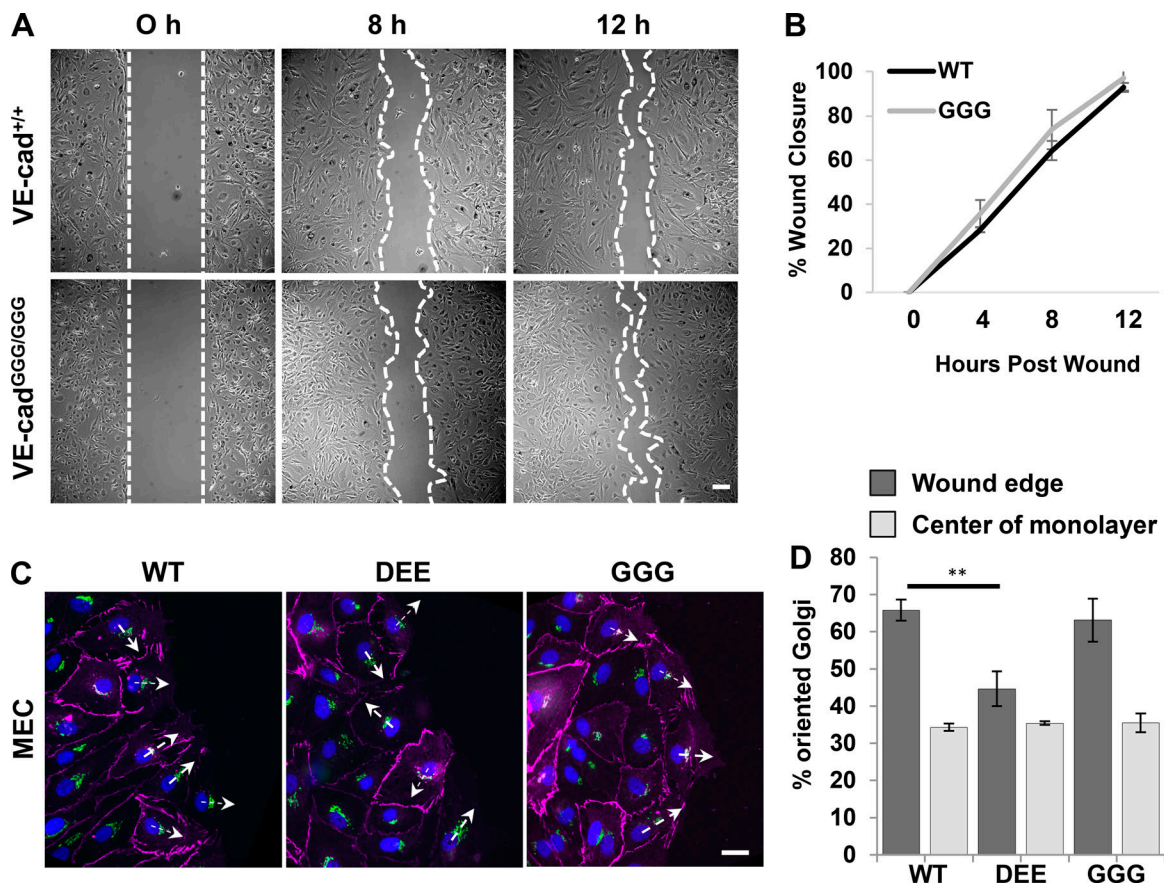


Figure S3. **Wounding assay with isolated VE-cad^{GGG/GGG} mutant cells and Golgi reorientation in human microvascular cells.** (A) Normal migration of isolated VE-cad^{GGG/GGG} mutant dermal endothelial cells in vitro. Scratch-wound assays were performed with primary dermal MECs isolated from VE-cad^{+/+} and VE-cad^{GGG/GGG} mutant mice. White dashed lines denote scratch borders. Scale bar: 100 μ m. (B) The percentage wound closure by VE-cad^{+/+} and VE-cad^{GGG/GGG} mutant cells was calculated over 12 h using phase-contrast microscopy. Graph shows the relative mean \pm SD and is representative of two independent experiments. (C) Golgi reorientation defects in human MECs expressing VE-cad^{DEE} mutant. Human MECs were adenovirally transduced with the indicated RFP tagged VE-cad constructs. Cells were fixed 6 h after wounding and immunostained for RFP (magenta), GM-130 (green), and nuclei (blue) to visualize reorientation of the Golgi toward the wound edge. Arrows indicate the nucleus-Golgi polarity axis. Scale bar, 25 μ m. (D) Graph shows the average percentage \pm SEM of RFP-positive cells with a polarized Golgi apparatus (in a 90° quadrant toward the wound edge) 6 h after wounding. At least 60 cells were analyzed for each condition. Graph represents average \pm SEM calculated from three independent experiments. **, $P < 0.005$, one-way ANOVA with Tukey post hoc test.

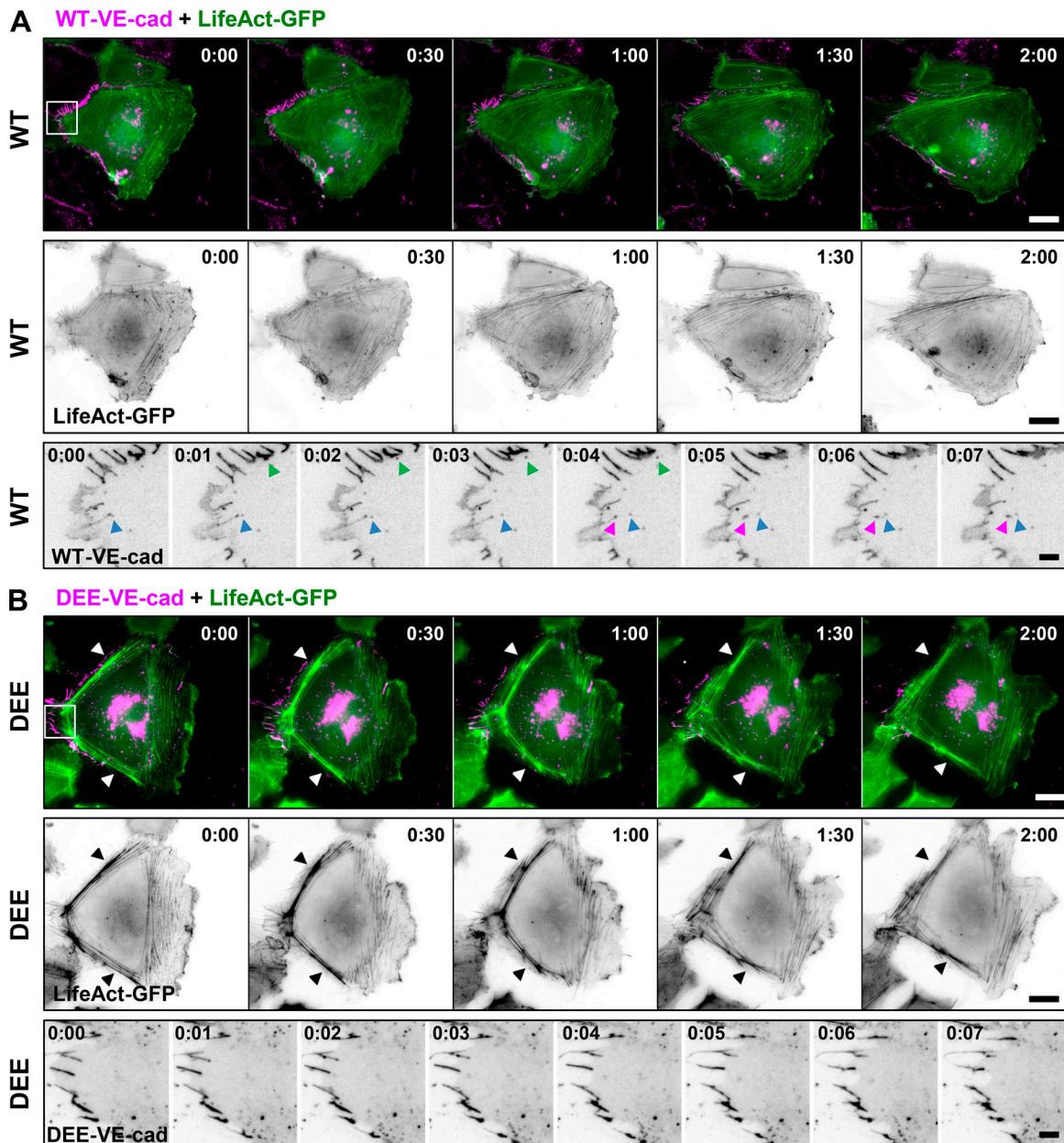


Figure S4. **Representative time-lapse images from wound edge HUVEC cells expressing LifeAct-GFP and either VE-cadWT-RFP or VE-cadDEE-RFP.** **(A)** Top, representative time-lapse images show a wound-edge HUVEC transduced with LifeAct-GFP (green) and VE-cadWT-RFP (magenta). The cell is surrounded by other cells, except for the wound edge on the right. Images were taken every minute for 2 h, beginning 1 h after wounding. Middle, images show normal LifeAct-GFP dynamics as cell migrates into scratch wound. Bottom, inset shows VE-cadWT-RFP-containing vesicles budding off from cell-cell junctions at the rear of the cell. Colored arrowheads indicate individual vesicles that have budded off from the plasma membrane. Time scale: hh:mm; scale bar (top, middle): 25 μ m, (bottom): 5 μ m. **(B)** Top, time-lapse images of HUVEC at the wound edge transduced with LifeAct-GFP (green) and VE-cadDEE-RFP (magenta). Middle, images show persistence of thick cortical actin bundles over 2-h imaging period (arrowhead). Bottom, inset from top panel shows decreased budding of VEcadDEE-RFP mutant from the rear of the cell. Budding was reduced by 44% in VEcadDEE-RFP-expressing cells compared with VEcadWT-RFP cells ($P < 0.05$, t test). Time scale: hh:mm; scale bar: (top, middle), 25 μ m; (bottom), 5 μ m.

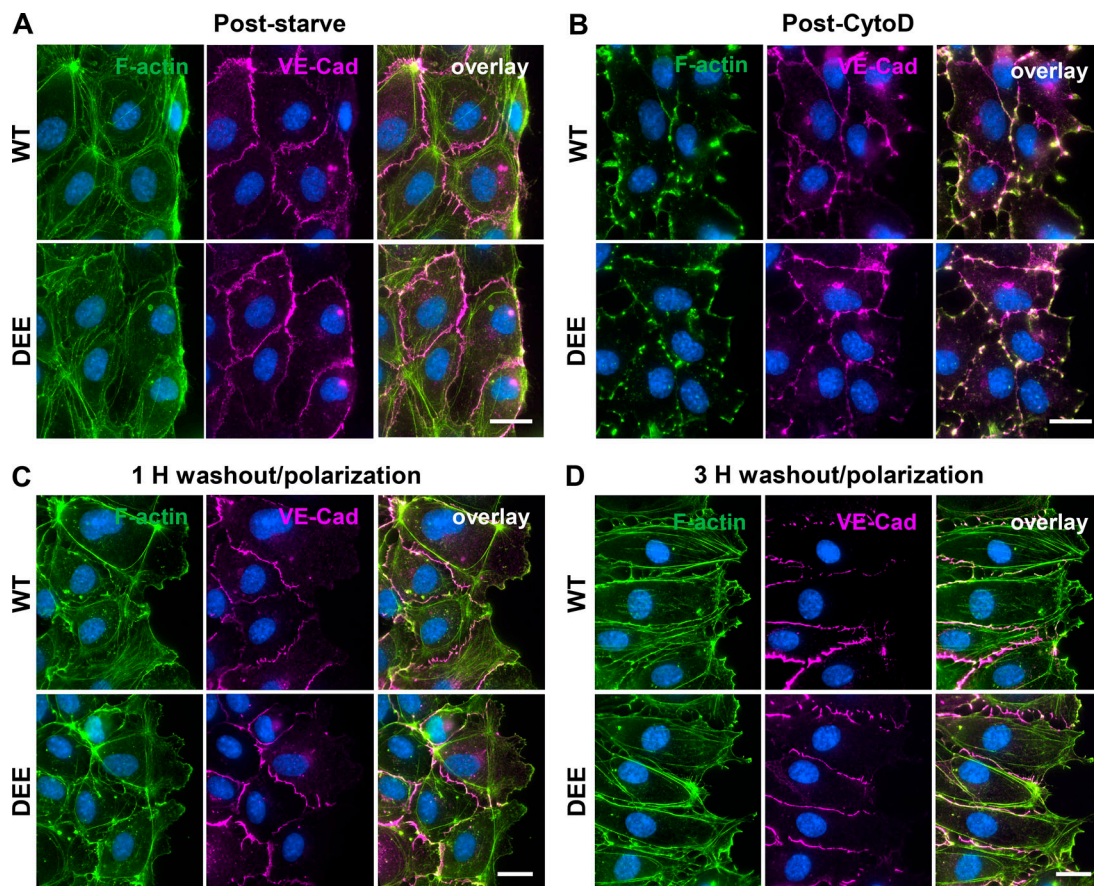


Figure S5. **Individual channels from cells shown in Fig. 8 D.** Individual channels from cells shown in Fig. 8 D stained for F-actin (green), VE-cad (magenta), and DAPI (blue). **(A)** Cells were starved, scratched, and immediately fixed. **(B)** Cells were fixed immediately after CytoD treatment. **(C and D)** Cells were fixed at the indicated time points during CytoD washout. Scale bar: 20 μm .